

Electronic Thesis and Dissertation Repository

---

8-6-2015 12:00 AM


## Thermal kinetics of ion irradiation hardening in selected alloys for the Canadian Gen. IV nuclear reactor concept

Heygaan Rajakumar  
*The University of Western Ontario*

Supervisor  
Dr. Robert Klassen  
*The University of Western Ontario*

Graduate Program in Mechanical and Materials Engineering  
A thesis submitted in partial fulfillment of the requirements for the degree in Master of Engineering Science  
© Heygaan Rajakumar 2015

Follow this and additional works at: <https://ir.lib.uwo.ca/etd>

 Part of the [Materials Science and Engineering Commons](#), [Nanoscience and Nanotechnology Commons](#), and the [Nuclear Engineering Commons](#)

---

### Recommended Citation

Rajakumar, Heygaan, "Thermal kinetics of ion irradiation hardening in selected alloys for the Canadian Gen. IV nuclear reactor concept" (2015). *Electronic Thesis and Dissertation Repository*. 3055.  
<https://ir.lib.uwo.ca/etd/3055>

This Dissertation/Thesis is brought to you for free and open access by Scholarship@Western. It has been accepted for inclusion in Electronic Thesis and Dissertation Repository by an authorized administrator of Scholarship@Western. For more information, please contact [wlsadmin@uwo.ca](mailto:wlsadmin@uwo.ca).

Thermal kinetics of ion irradiation hardening in selected alloys for the Canadian  
Gen. IV nuclear reactor concept

(Thesis format: Monograph)

by

Heygaan Rajakumar

Graduate Program in Mechanical and Materials Engineering

A thesis submitted in partial fulfillment  
of the requirements for the degree of  
Master of Engineering Science

The School of Graduate and Postdoctoral Studies  
The University of Western Ontario  
London, Ontario, Canada

© Heygaan Rajakumar 2015

## Abstract

Canada is designing supercritical water fission reactors (SCWR) to increase the thermal efficiency of nuclear power generation from ~34% to ~48%. The temperature and pressure of a supercritical water reactor core is very high compared to a CANDU reactor. This thesis examines irradiation hardening and thermal recovery of two candidate alloys, AISI 310 and Inconel 800H, for the Canadian SCWR.

Samples of both alloys are mechanically ground and polished, then irradiated using 8.0 MeV Fe ions. The use of ion irradiation safely and quickly simulates neutron damage. The change in the hardness of the samples is then studied during a series of thermal anneals at temperatures ranging from 400° to 600° C.

This study found virtually all irradiation-induced hardening had recovered within 100 minutes of exposure to these temperatures.

## Keywords

ion implantation, ion irradiation, thermal recovery, supercritical water reactors, nano-indentation, micro-indentation

## Acknowledgments

I could not have written this thesis without the invaluable insight, wisdom, guidance, and hard work of several people.

First and foremost, I'd like to thank, Professor Robert J. Klassen for his mentorship and confidence in me. Additionally, I'd like to thank Dr. Vineet Bhakhri for his assistance in designing and running experiments.

I'd like to thank NSERC, Canmet, and CNL for their assistance, their support, and most importantly the opportunity to investigate irradiation damage and recovery for the Gen. IV initiative.

# Table of Contents

Abstract .....	ii
Table of Contents .....	iv
Figures.....	vii
Tables .....	xii
Chapter 1 .....	1
1    Introduction.....	1
Chapter 2.....	3
2    Review of the literature.....	3
2.1    The Canadian Gen. IV SCWR concept.....	3
2.1.1    SCWR layout .....	3
2.1.2    Operation of the Canadian Gen. IV SCWR .....	3
2.2    Neutron/ion irradiation induced crystallographic damage.....	6
2.2.1    Neutron and ion irradiation.....	8
2.2.2    Calculating ion irradiation dosage .....	12
2.2.3    Effect of neutron/ion irradiation on material properties .....	14
2.2.4    Neutron and ion irradiation summary .....	16
2.3    Thermally-activated recovery of irradiation damage.....	16
2.4    Measuring the rate of thermal recovery of mechanical properties .....	19
2.4.1    Stress relaxation testing .....	19

2.4.2	Micro-mechanical indentation testing.....	20
2.4.3	Depth dependence of micro-indentation hardness .....	23
2.5	Summary .....	26
Chapter 3.....		28
3	Experimental Procedure.....	28
3.1	Sample preparation .....	28
3.2	Ion Irradiation .....	31
3.3	Micro-indentation .....	33
3.4	Thermal annealing .....	36
Chapter 4.....		37
4	Experimental Results .....	37
4.1	Indentation hardness of the ion irradiated samples.....	37
4.2	Indentation hardness of the annealed samples .....	39
4.3	Oxidation during annealing.....	44
Chapter 5.....		48
5	Discussion .....	48
5.1	Effect of indentation depth on hardness.....	48
5.2	Effect of ion irradiation on hardness.....	50
5.3	Thermal recovery .....	54
5.3.1	Calculation of critical recovery time, $t_c$ .....	56

5.3.2	Model of the thermal recovery process.....	59
5.4	Testing issues and their effects .....	63
Chapter 6	.....	64
6	Conclusions.....	64
Works Cited		66

## Figures

Figure 2.1 Canadian SCWR layout.....	2
Figure 2.2 Canadian SCWR pressure tube horizontal section view .....	2
Figure 2.3 Canadian SCWR pressure tube lower vertical section view .....	3
Figure 2.4 Temperature-pressure phase diagram of water [4].....	3
Figure 2.5 Temperature-entropy diagram comparing supercritical and subcritical water Rankine cycles. The ratio of output work to output heat is much higher with supercritical coolant, meaning the thermal efficiency is higher with supercritical coolant relative to an equivalent a Rankine cycle with subcritical coolant. ....	4
Figure 2.6 Pressure tube assembly and temperature distribution. Fuel cladding and liner components experience the highest temperatures. The fuel cladding is also exposed to the highest neutron flux. ....	6
Figure 2.7 Irradiation effects on lattice structure. a) Before irradiation: high energy particle moving towards a lattice of low energy atoms. b) At collision: high energy particle impacts and dislocates a lattice atom. c) Cascade collisions: the PKA collides with and dislocates another atom. The radiation particle continues moving into the lattice, transferring more of its energy to other atoms. d) After collision: lattice now has stress concentrations, vacancies, interstitials, and may have substitutional defects and is in a higher energy state. ....	7
Figure 2.8 Representative TEM micrographs showing the development defects and dislocations in the microstructure of a zirconium foil with $\text{Kr}^{2+}$ ion irradiation damage ranging from 0.08 dpa to 0.8 dpa at 400° C [17]. ....	8
Figure 2.9 Percentage hardening of 316LN for various 3.5 MeV Fe irradiation doses at 200° C. The dose is given in peak displacement damage, which is the estimated sum of the induced damage, which most has mostly recombined. Hardness was recorded at 150 nm indentation depths. The shaded curve shows the trend and approximates scatter [9]. ....	10



Figure 2.10 Change in indentation hardness, normalized with respect to the hardness at 0 dpa, versus  $Zr^+$  ion irradiation damage for Zr-2.5%Nb. The indentation tests were performed on the axial normal (AN), radial normal (RN), and transverse normal (TN) planes of the pressure tube. The rate of irradiation hardening is clearly dependent upon the plane of indentation [28]..... 11

Figure 2.11 True stress versus true strain for ion irradiated (room temperature) tests, non-irradiated (room temperature) tests, and non-irradiated (high temperature) tests from uniaxial pillar compressions on an extruded Zr-2.5%Nb pressure tube in the a) transverse, b) radial, and c) the axial pressure tube directions [29]..... 12

Figure 2.12 Dislocations of 8.0 MeV Fe ions irradiating pure Fe. This shows the dislocations and cascade dislocations of 100 simulated ions..... 14

Figure 2.13 Interstitial and vacancy dislocation loops. The anisotropic stress on adjacent atomic planes causes a warp in the local lattice structure, increasing the energy required for dislocation and defect glide through the material to occur. .... 15

Figure 2.14 Four simple mechanisms by which atoms can move in a crystalline material a) the ring mechanism b) the vacancy mechanism c) the interstitial mechanism d) the interstitialcy mechanism. .... 17

Figure 2.15 Illustration of the energy,  $q$ , required for an atom to move towards an adjoining vacancy. If the thermal vibration energy  $\geq qm$  an atom can move into the vacancy..... 17

Figure 2.16 Recovery of the yield strength of single crystal zinc at 253 K and 283 K [39] ..... 19

Figure 2.17 Indentation force,  $P$ , versus indentation depth,  $h$ , for an elastic-plastic specimen [40]..... 21

Figure 2.18 Geometry of an axisymmetric conical indentation used by *Johnson* to calculate the relationship between the indentation plastic zone radius “ $c$ ” and the indentation width “ $a$ ” (Equation 2.15) [43]. .... 22

Figure 2.19 Evidence of depth dependence of the hardness of single crystal and cold worked, polycrystalline Cu using micro-indentation with a diamond Berkovich indenter [49].	24
Figure 2.20 McElhaney's data from Figure 2.19 replotted by Nix and Gao [48].	25
Figure 3.1 Microstructure of AISI 310 observed with an optical microscope.	30
Figure 3.2 Microstructure of Inconel 800H observed with an optical microscope. ....	30
Figure 3.3 Schematic illustration of the Tandetron ion accelerator located at the University of Western Ontario [49].	31
Figure 3.4 Schematic illustration of typical regions of ion exposure for samples used in this experiment.	32
Figure 3.5 Schematic illustration of the NanoTest indentation hardness testing platform that was used in this study. ....	33
Figure 3.6 Indentation force versus depth and corresponding indentation hardness, $H = P/A$ , versus depth curves from a typical indentation test performed in this study. In this plot $H$ is calculated from the <i>total</i> indentation depth. The partial unloading performed at indentation depth increments of 100 nm are shown. The slope of these unloadings are used to determine the plastic indentation depth $h_p$ from which the actual hardness is calculated using Equations 2.10 - 2.12.	34
Figure 3.7 Optical image of fourteen indentations from a $7 \times 2$ indentation array. ....	35
Figure 4.1 Indentation hardness measured over a range of indentation depth for non-irradiated AISI 310. ....	37
Figure 4.2 Indentation hardness measured over a range of indentation depth for non-irradiated Inconel 800H. ....	38

Figure 4.3 Indentation hardness measured over a range of indentation depth for Fe<sup>4+</sup> irradiated AISI 310 samples before thermal recovery. .... 40

Figure 4.4 Indentation hardness measured over a range of indentation depth for Fe<sup>4+</sup> irradiated Inconel 800H before thermal recovery ..... 41

Figure 4.5 Indentation hardness measured over a range of indentation depth for samples that were annealed for various times and temperatures for: a) non-irradiated AISI 310; b) 0.1 dpa irradiated AISI 310; c) 1 dpa irradiated AISI 310..... 42

Figure 4.6 Indentation hardness measured over a range of indentation depth for samples that were annealed for various times and temperatures for: a) non-irradiated Inconel 800H; b) 0.1 dpa irradiated Inconel 800H; c) 1 dpa irradiated Inconel 800H. .... 43

Figure 4.7 Ion irradiated test samples exposed to 400° C for 1000 minutes. a) Optical low magnification images of AISI 310 (left) and Inconel 800H (right) b) High magnification, optical image of Inconel 800H sample c) High magnification, optical image of AISI 310 sample. These images show clearly that the extent of oxidation is reduced in regions exposed to high levels of ion irradiation. .... 45

Figure 4.8: Relative hardness for 1 dpa irradiated AISI 310 during 10 minutes of recovery. This shows softening occurred for the first minute from 400° to 600° C. After 1 minute, the samples recovering at 500° and 600° C harden. This phenomenon occurs for all irradiation levels, including non-irradiated samples, in both AISI 310 and Inconel 800H most strongly at 500° C. The 500° C was recovered with shorter purges, which correlates with the more intense hardening. .... 47

Figure 5.1 Depth-hardness data from non-irradiated test samples plotted as ***HHo2*** over ***1hp*** to examine the indentation depth dependence of hardness on the test materials. .... 49

Figure 5.2 Schematic illustration of a hemispherical plastic deformation zone, of radius *c*, around an indentation of width *a*. .... 50

Figure 5.3 Change in indentation hardness ( $\Delta H$ ) at 200 nm indentation depth, versus irradiation dose (displacements per atom or dpa) for the AISI 310 and Inconel 800H samples of this study. Data from Fe ion irradiated AISI 316LN reported by *Hunn et al.* [9] are also included in this plot. Trend lines for Equations 5.5a - 5.5c have been plotted alongside the data..... 52

Figure 5.4 Relative hardness for AISI 310 during recovery at 400° C. The plot show consistent softening towards the average non-irradiated, polished hardness. In the case of the 0.1 dpa hardness averaging below 1, this can be attributed to the removal of most of the irradiation hardening damage as well as the cold work from polishing which is present in all unrecovered hardness values. .... 55

Figure 5.5  $t_c$  versus irradiation dose (dpa) for AISI 310 and Inconel 800H during recovery, under the premise that  $t_c$  occurs when 99% of irradiation hardening has dissipated. .... 58

Figure 5.6 A comparison of the experimental AISI 310 data and the model for AISI 310 (Equation 5.18a)..... 61

Figure 5.7 A comparison of the experimental Inconel 800H data and the model for Inconel 800H (Equation 5.18b)..... 62

## Tables

Table 3.1: Chemical composition, in weight percentage, of the Inconel 800H and AISI 310 alloys [11, 12] .....	28
Table 3.2: Test matrix for this study. The circles indicate tests performed on AISI 310 samples while the squares indicate tests performed on Inconel 800H samples.....	32
Table 5.1: Bulk hardness and characteristic length for various materials, including this experiments test materials, AISI 310 and Inconel 800H [48, 53, 54].....	50
Table 5.2: Comparison of coefficient and exponential values to describe irradiation hardening of AISI 310 and Inconel 800H against the findings of <i>Hunn et al.</i> for AISI 316LN in the form of Equation 5.3. See Equations 5.5a - 5.5c. [9] .....	53
Table 5.3 lists the calculated values of <b><i>A</i></b> and <b><i>n</i></b> parameters of Equation 5.7 for AISI 310 and Inconel 800H samples irradiated to various dpa levels and annealed at the various temperatures. Note: italicized parameters indicate a hardening from thermal exposure. These values indicate high surface oxidation of the sample as described in Section 4.3. Bold parameters represent tests where surface oxidation was minimal. Bold data are used to predict the rate of thermal recovery of irradiation hardening. ....	57

# Chapter 1

## 1 Introduction

The majority of existing nuclear reactors, including Canadian CANDU reactors, utilize liquid water cooling. This limits their thermal efficiency to between 33 and 37% [1]. The electrical generation industry is moving to the use of supercritical water cooling ( $T > 374^\circ \text{C}$  and  $P > 22 \text{ MPa}$ ) to improve the thermal efficiency to greater than 48%. Supercritical Water Reactors (SCWRs) powered by fossil fuel combustion (coal and natural gas) are now being used throughout the world [2].

The Canadian nuclear industry has begun preliminary research to develop a heavy-water moderated nuclear SCWR. This next generation (Gen. IV) reactor will replace the existing CANDU reactors. The fact that the temperature and the neutron flux, within the core of a Gen. IV SCWR will be considerably higher than in the core of current CANDU reactors presents considerable challenges for selecting suitable reactor core materials. In particular, the combined effect of neutron irradiation hardening and thermal softening of the candidate alloys at the temperature and neutron flux levels within the Gen. IV SCWR core has not been studied.

This thesis presents the results of a study which uses high energy Fe ion irradiation, to simulate neutron irradiation, and post-irradiation annealing to assess the combined effect of neutron irradiation and thermal recovery on the mechanical hardness of two Fe-based alloys that are being considered for in-core applications in the Canadian Gen. IV SCWR. The hypotheses upon which this study is based are the following:

1. High energy Fe ion irradiation will produce similar crystallographic damage, to a depth of about  $2 \mu\text{m}$ , as fast neutron irradiation. Thus, Fe ion irradiation can be used as a simulation the hardening induced by neutron irradiation for Fe-based alloys.
2. The development of irradiation damage and the thermal recovery of the damage, occur by independent mechanisms; therefore, we will irradiate samples to different levels of crystallographic damage and then anneal the samples at various temperatures for

- various duration to establish separate empirically-based expressions for the rates of damage accumulation and rate of thermal recovery of the damage.
3. These two expressions can then be applied to predict the rate at which the hardness of the selected alloys will change with neutron irradiation fluence, temperature, and time over the range expected for specific in-core components of a Gen. IV SCWR.

This thesis consists of seven chapters. Chapter 2 contains a review of the literature dealing with the key concepts pertaining to this study. Chapter 3 presents details on the experimental procedures used in this study. The results obtained from these experiments are presented in Chapter 4. A discussion of the results, including an analysis of their precision and demonstrations of their application, is presented in Chapter 5. Chapter 6 presents the conclusions of this study. Chapter 7 provides suggestions for future work arising from the findings of this research.

Results of this study were published in the ASME Journal of Nuclear Engineering and Radiation Science (currently in press, Paper #: NERS-15-1077) and presented at the 25<sup>th</sup> CANSAM conference (London, ON, 2015), the 7<sup>th</sup> International Symposium on Supercritical Water-Cooled Reactors (Helsinki, Finland 2015), the Materials Science and Technology Conference (Montreal, PQ, 2013), and the 25<sup>th</sup> Canadian Materials Science Conference (Montreal, PQ, 2013).

# Chapter 2

## 2 Review of the literature

The objective of this study is to assess the effect of high energy neutron irradiation and thermal recovery on the mechanical hardness of two Fe-based alloys that are being considered for certain critical components within a Gen. IV SCWR core. To put this research into proper context, it is necessary to provide background information on several key topics related to the proposed Gen. IV reactor and to the mechanisms of irradiation induced hardening and temperature induced recovery of hardness in crystalline metals.

Section 2.1 provides a brief description of the general layout and operation of the proposed Canadian Gen. IV SCWR core. Section 2.2 describes the characteristics of the type of crystallographic damage that is caused in metals as a result of neutron and heavy ion irradiation. The similarities between those two types of irradiation are demonstrated. Section 2.3 illustrates the mechanisms through which thermal recovery of crystallographic damage occurs in metals. Section 2.4 concludes this literature review, by examining micromechanical testing techniques which have been developed to measure the local mechanical strength and hardness at the nano-meter length scale. These techniques will be applied in this study to assess the properties of the ion-irradiated/annealed test samples.

### 2.1 The Canadian Gen. IV SCWR concept

#### 2.1.1 SCWR layout

The design of Canada's proposed Gen. IV SCWR has many fundamental similarities to existing CANDU reactor design. Like a CANDU reactor, the Gen. IV SCWR has a calandria vessel containing many fuel channels surrounded by heavy water ( $D_2O$ ) which acts as the neutron moderator. Each fuel channel consists of a pressure tube containing the nuclear fuel bundles and  $H_2O$  coolant to transport the generated fission heat from the core (Figure 2.1).



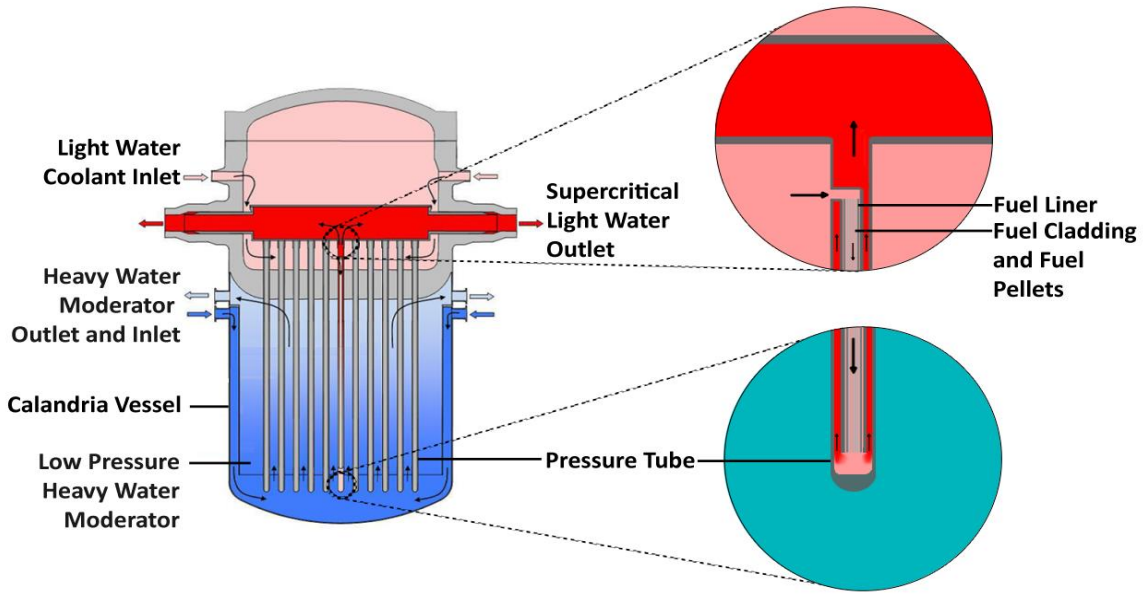


**Figure 2.1 Canadian SCWR layout**

Unlike the CANDU layout, the fuel channels in the Gen IV SCWR core are aligned vertically rather than horizontally. The pressure tubes are designed to support significant hoop stress generated by the internal pressure of the H<sub>2</sub>O coolant and are protected from the high coolant temperature by metal fuel liners and ceramic thermal insulating layers (Figures 2.2, 2.3).

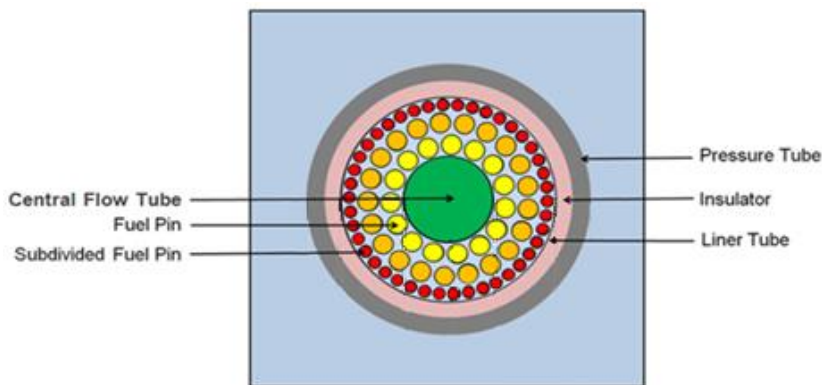


**Figure 2.2 Canadian SCWR pressure tube horizontal section view**

### 2.1.2 Operation of the Canadian Gen. IV SCWR

Within the pressure tube the H<sub>2</sub>O coolant runs first downward through a central flow tube and then upward through the fuel bundles (Figure 2.3). The fuel bundles contain numerous fuel pins consisting of stacks of fuel pellets encased in metal cladding to prevent mixing of radioactive fuel/fission products with the coolant [3].

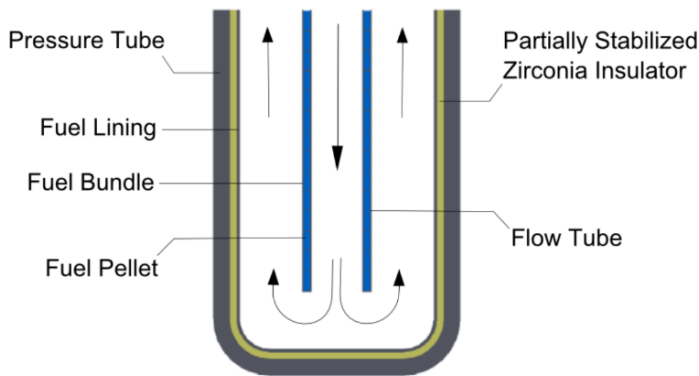


**Figure 2.3 Canadian SCWR pressure tube lower vertical section view**

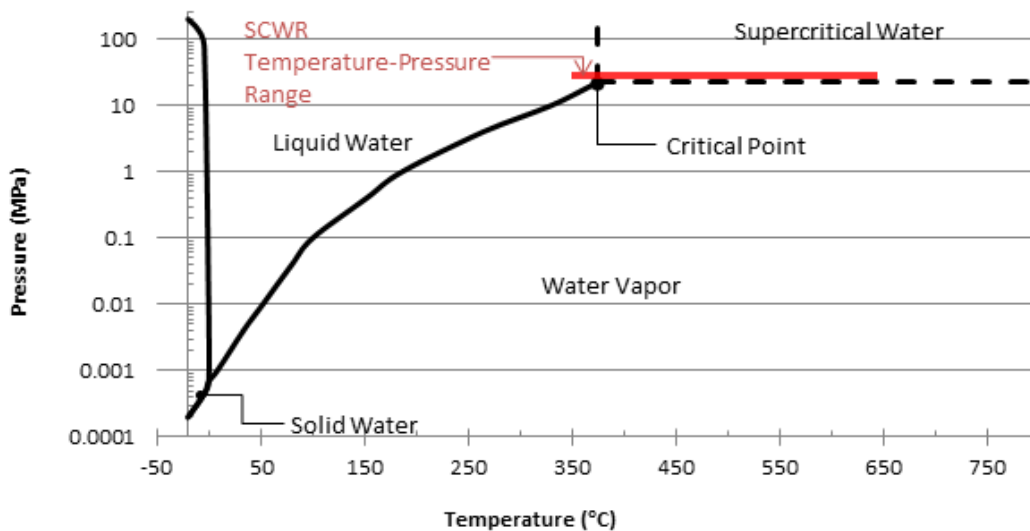


**Figure 2.4 Temperature-pressure phase diagram of water [4]**

Supercritical water occurs when the temperature and pressure is above 374° C and 22.06 MPa (Figure 2.4). The H<sub>2</sub>O coolant enters the pressure tubes at 25 MPa of pressure

and temperatures of 350° C. The coolant heats up as it passes over the fuel bundles to reach 800° C and 25 MPa as it exits the pressure tube. The exiting water is therefore well within the supercritical water state [3]. The metal fuel liner and the fuel cladding are the metal components within the Gen IV core that are exposed to the highest temperature and neutron flux thus safe operation of this reactor is absolutely dependent on their ability to endure these extreme conditions.

Temperature-entropy diagrams can depict the enhanced thermal efficiency available when a Rankine cycle, analogous to the thermodynamic coolant cycle of a nuclear generating station, is operated with supercritical rather than subcritical water coolant (Figure 2.5).

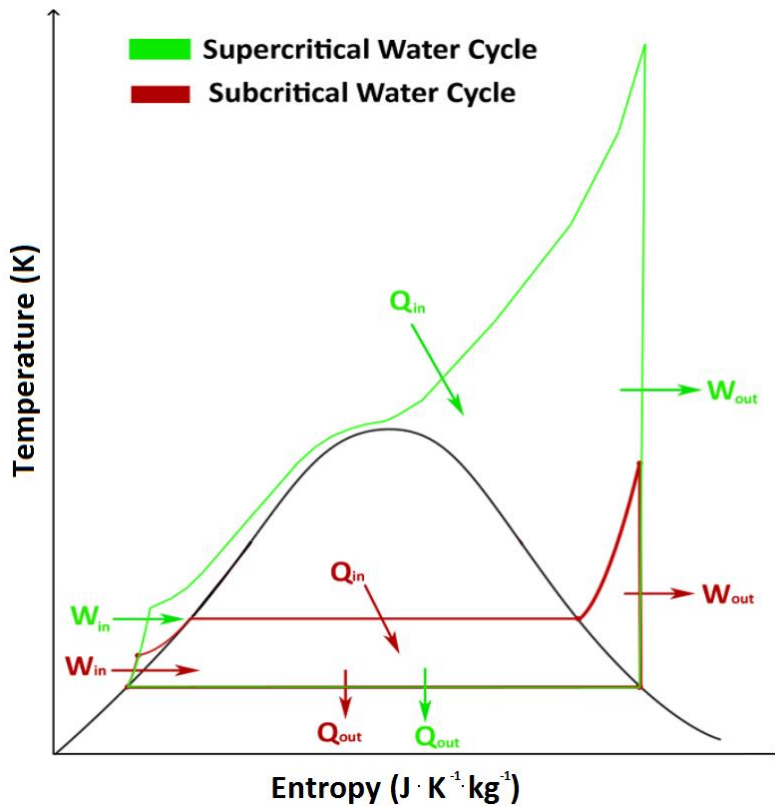


**Figure 2.5 Temperature-entropy diagram comparing supercritical and subcritical water Rankine cycles. The ratio of output work to output heat is much higher with supercritical coolant, meaning the thermal efficiency is higher with supercritical coolant relative to an equivalent a Rankine cycle with subcritical coolant.**

In the Rankine cycle of a nuclear fission reactor, energy enters and leaves the system through work input ( $W_i$ ), heat input ( $Q_i$ ), work output ( $W_o$ ), and heat output ( $Q_o$ ). The  $W_i$  is the work, applied by a pump, to pressurize the coolant and create flow. The  $Q_i$  is the fission heat absorbed by the coolant.  $W_o$  is the energy generated by the turbines and  $Q_o$  is the “wasted” heat energy resulting from inefficiencies in the actual cycle. Decreasing the  $Q_o/W_o$  ratio will increase the thermal efficiency,  $\eta_{th}$  (Equation 2.1).

$$\eta_{th} = \frac{W_o}{W_i+Q_i} = \frac{W_o}{W_o+Q_o} = \frac{1}{1+\frac{Q_o}{W_o}} \quad 2.1$$

The higher efficiency of a SCWR equates to less associated fuel costs and less generated nuclear waste. It has been estimated the thermal efficiency of Canada's Gen IV SCWR design will be 48% through the thermodynamic benefits of supercritical water coolant operating at 25 MPa and between approximately 350° to 800° C [5]. This is a significant improvement when compared to the 34% thermal efficiency of CANDU technology in use today [6].

The conditions within the core of the Canadian Gen IV SCWR will be harsher than those within the core of a CANDU reactor due to the much higher coolant temperature and pressure ranges as well as the relatively corrosive nature of supercritical water compared to traditional light water coolants. The critical metal components in the reactor core are the fuel liner and the fuel cladding (Figure 2.6).

The metal liner remains in the core throughout the reactor's lifetime, unlike the fuel cladding, which will be removed with the fuel bundles during refuelling. Therefore the metal liner will experience very long exposures to high temperature and neutron irradiation.

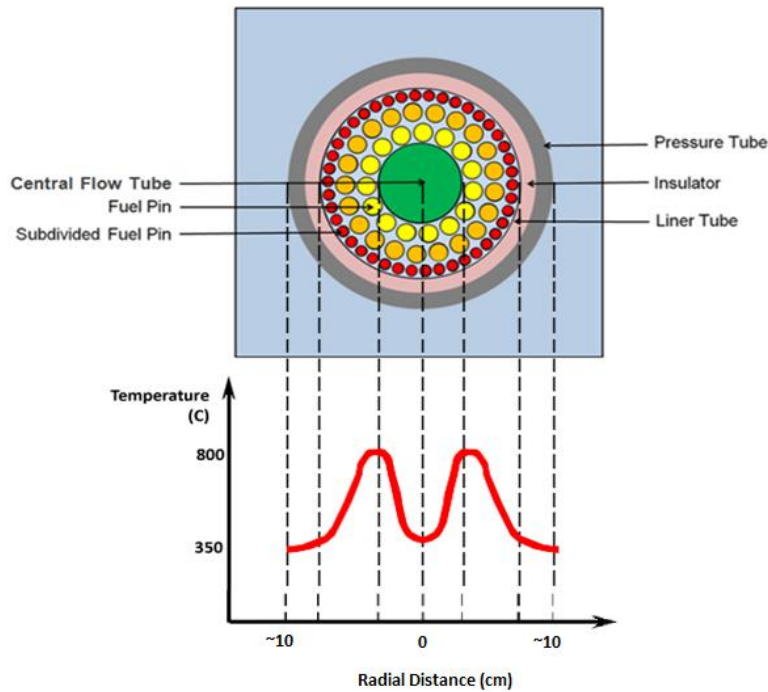


**Figure 2.6 Pressure tube assembly and temperature distribution. Fuel cladding and liner components experience the highest temperatures. The fuel cladding is also exposed to the highest neutron flux.**

The liner and cladding require metal alloys of high strength and creep resistance up to 800° C [7]. Two candidate alloys for these components are the high temperature application, ferrous alloys, Inconel 800H and AISI 310 (See Table 3.1) [8-10]. While the high temperature strength and creep resistance of these materials in their non-irradiated form is well studied and their service temperature extends up to 800° C [11, 12], the effect of neutron irradiation hardening on these properties is still under investigation and providing data on this subject is the objective of this thesis.

## 2.2 Neutron/ion irradiation induced crystallographic damage

Neutron and ion irradiation have the general effect of hardening and embrittling crystalline metals [13-16]. A periodic, crystalline arrangement of atoms has a characteristic hardness, which is fundamentally based upon the electronic structure and inter-atomic bond strength

of the atoms. Bombarding this lattice with high energy particles will dislocate atoms from their lattice sites, forming vacancy and interstitial type point defects [17-19]. The atoms that are dislocated by direct particle impact are referred to as primary knock-on atoms (PKA) and often dislocate more atoms through secondary and tertiary collisions. These dislocated atoms accumulate to form "vacancy" and "interstitial" type dislocation loops (Figure 2.7). This type of irradiation damage appears as a uniform distribution of small, less than about 10 nm diameter, dislocation loops throughout the irradiated material, and is quantified as an average number of displacements per atom (dpa). Figure 2.8 shows high magnification electron microscope images of the irradiation, visible as a uniform distribution of diffuse black dots, in a Zr sample that was irradiated with  $\text{Kr}^{2+}$  ions.

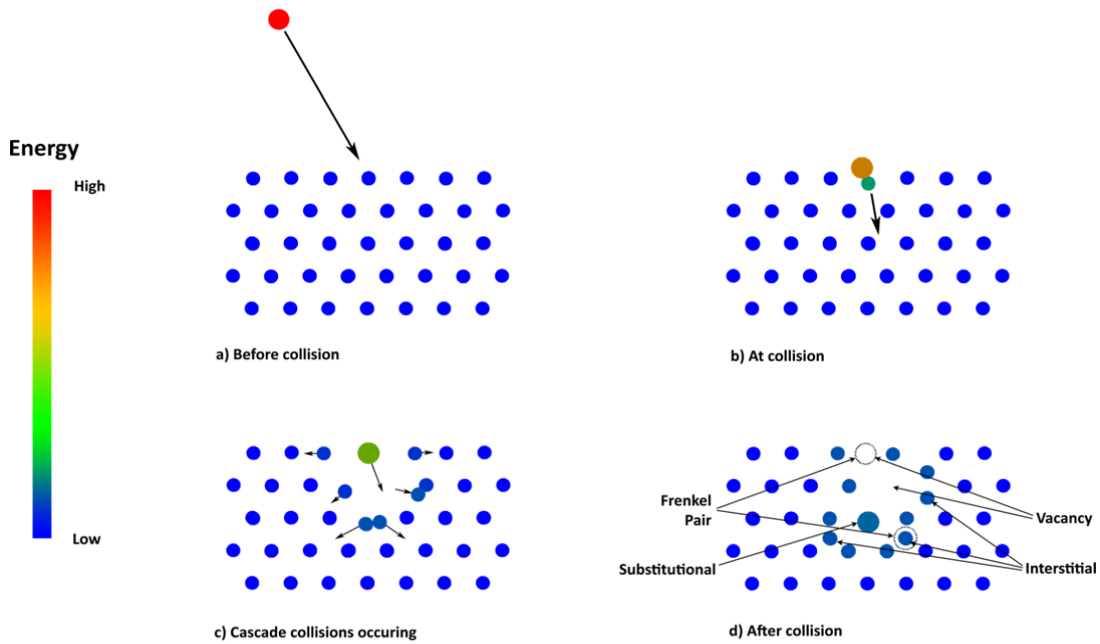


**Figure 2.7 Irradiation effects on lattice structure. a) Before irradiation: high energy particle moving towards a lattice of low energy atoms. b) At collision: high energy particle impacts and dislocates a lattice atom. c) Cascade collisions: the PKA collides with and dislocates another atom. The radiation particle continues moving into the lattice, transferring more of its energy to other atoms. d) After collision: lattice now has stress concentrations, vacancies, interstitials, and may have substitutional defects and is in a higher energy state.**

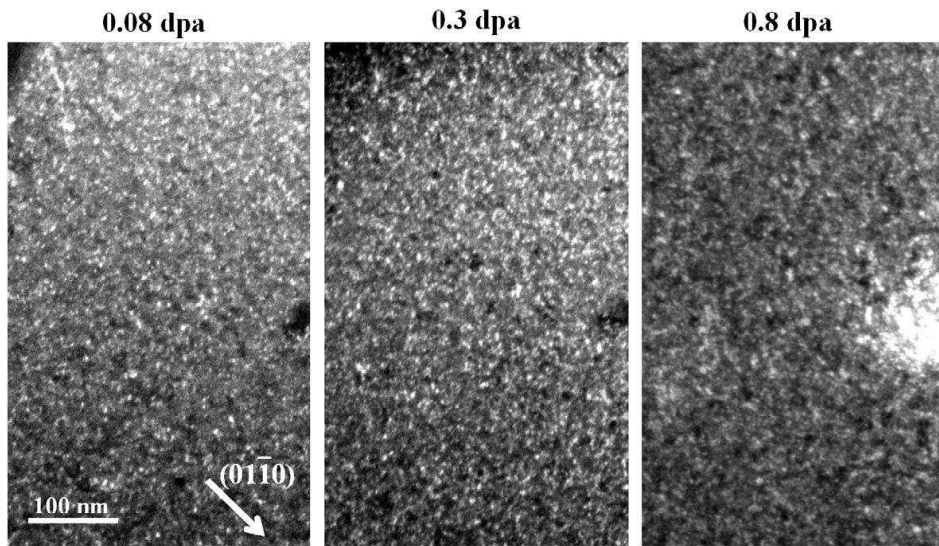


**Figure 2.8 Representative TEM micrographs showing the development defects and dislocations in the microstructure of a zirconium foil with  $\text{Kr}^{2+}$  ion irradiation damage ranging from 0.08 dpa to 0.8 dpa at 400° C [17].**

### 2.2.1 Neutron and ion irradiation

High energy, heavy ion irradiation is a fast, safe, and an economical means to simulate neutron irradiation damage [9, 20, 21]. Presently, irradiation studies often use self-similar ion irradiation in lieu of neutron irradiation [20 - 25]. Like neutron irradiation, heavy ion irradiation results in displacement of atoms from their usual crystal lattice positions and hence creates point defects within the target material. Unlike neutron irradiation, heavy ion interaction does not change the internal energy state of the nuclei of the target atoms and hence the target sample does not become radioactive as a result of the ion irradiation. This allows safe examination after irradiation. The large size and high kinetic energy (in the MeV energy range) also results in heavy ion irradiation imparting irradiation damage at rates orders of magnitude higher than neutron irradiation would; for example, several hours of high flux irradiation of an Fe-based alloy with 8 MeV  $\text{Fe}^{4+}$  ions such as those used in this thesis research, will impart the same amount of crystal damage, about 30 displacements

per atom (dpa), as a structural in-core component would experience in a 30 year life time in a typical thermal neutron reactor core [26]. This illustrates the very significant practical benefits of using heavy ion irradiation to simulate neutron irradiation in the testing of nuclear materials.

Despite the many similarities between the crystal damage created by heavy ion and fast neutron irradiation difference do exist between the two irradiation sources [23, 26]. Most significantly, the large size and charge of the ions results in very shallow depth of penetration into the target material compared to that of neutrons. This means that if ion-irradiation is to be used to simulate neutron irradiation, micro-mechanical testing techniques must be used to test the shallow (typically less than 3  $\mu\text{m}$  depth) ion-affected zone [20, 22, 24, 25, 27].

Several examples of nano-indentation hardness testing on high-energy, self-similar ion irradiated material have illustrated the capabilities of this type of testing for structural nuclear materials [9, 28, 29].

Oak Ridge National Laboratories has studied irradiation hardening in this manner a number of times. During one such study, AISI 316LN was exposed to 3.5 MeV Fe ion damage and studied using a nano-indenter. The study showed ion irradiation hardens AISI 316LN, but also that as ion dose increased, the percent hardening converged to a saturation point (Figure 2.9). This data implies hardness and irradiation dose have a power law relationship [9].



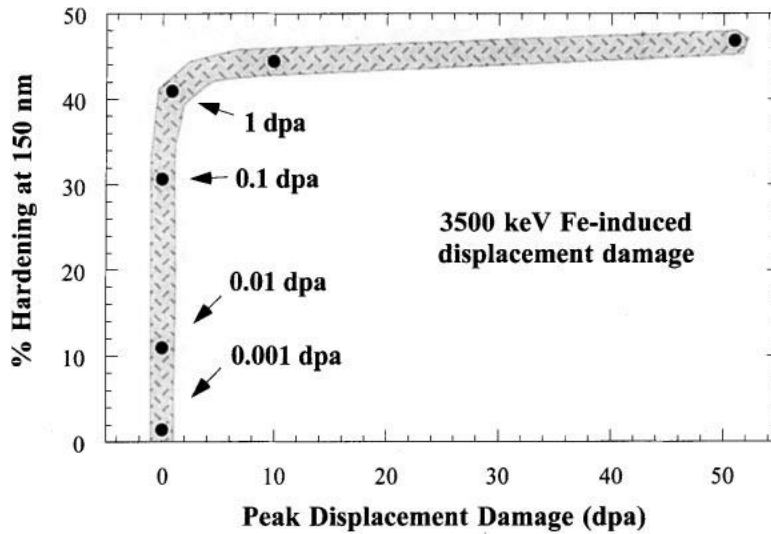


**Figure 2.9 Percentage hardening of 316LN for various 3.5 MeV Fe irradiation doses at 200° C. The dose is given in peak displacement damage, which is the estimated sum of the induced damage, which most has mostly recombined. Hardness was recorded at 150 nm indentation depths. The shaded curve shows the trend and approximates scatter [9].**

The nano-indentation hardness of  $Zr^+$  ion irradiated Zr-2.5%Nb (CANDU pressure tube material) was used to better understand the effects of irradiation-induced dislocation loops on the dislocation glide mechanism governing the operative plastic deformation process of CANDU pressure tubes at 250° to 310° C [28]. Figure 2.9 illustrates a key finding of this study; namely, the hardness of the pressure tube material increases with irradiation and the rate of increase is different along different directions of the tube. Transmission Electron Microscopy (TEM) indicated that the hardening was caused by nano-meter sized dislocation loops that resulted from the  $Zr^+$  irradiation, and this is similar to what occurs when Zr-2.5%Nb is exposed to either neutron irradiation or  $Kr^{2+}$  irradiation (Figure 2.8).

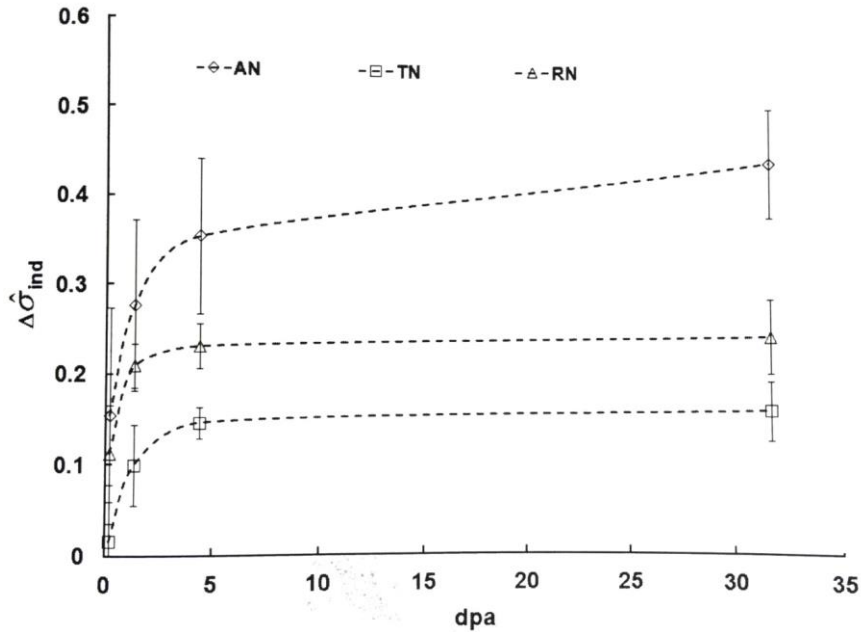


**Figure 2.10 Change in indentation hardness, normalized with respect to the hardness at 0 dpa, versus  $Zr^+$  ion irradiation damage for Zr-2.5%Nb. The indentation tests were performed on the axial normal (AN), radial normal (RN), and transverse normal (TN) planes of the pressure tube. The rate of irradiation hardening is clearly dependent upon the plane of indentation [28].**

The findings reported in [28] and shown in Figure 2.10 were pursued further by Oviasuyi and Klassen, who studied in more detail the effect of temperature and irradiation hardening on the mechanical anisotropy of Zr-2.5%Nb CANDU pressure tube material using self-similar Zr ion irradiation. They employed spherical-indentation hardness testing, and uniaxial compression tests performed with micro-pillars made from the ion irradiated material [29]. The tests were performed with micro-pillars aligned along the axial, radial, and transverse directions of the pressure tube at temperatures between 25° and 300° C. The stress-strain curves obtained from this study confirmed that the ion irradiation induced hardening of the pressure tube material was directionally anisotropic with the percentage hardening in the transverse direction being less than that in the radial and the axial directions (Figure 2.11) [29].

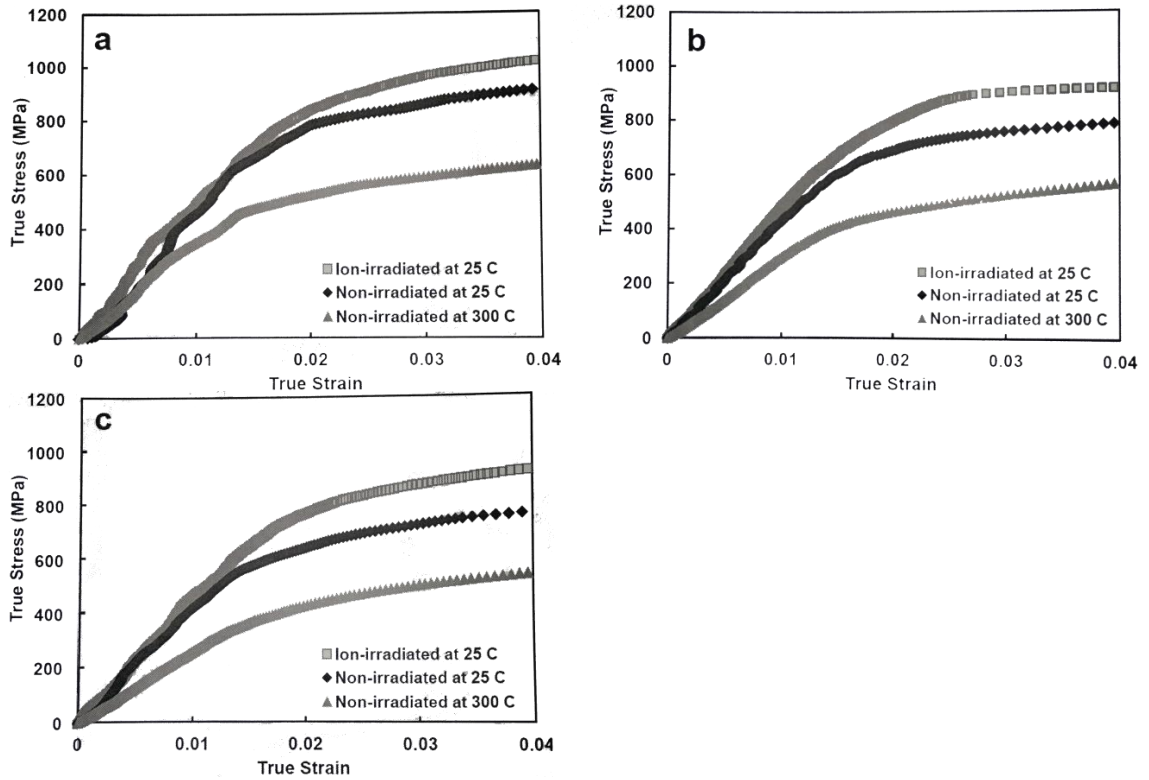


**Figure 2.11 True stress versus true strain for ion irradiated (room temperature) tests, non-irradiated (room temperature) tests, and non-irradiated (high temperature) tests from uniaxial pillar compressions on an extruded Zr-2.5%Nb pressure tube in the a) transverse, b) radial, and c) the axial pressure tube directions [29].**

### 2.2.2 Calculating ion irradiation dosage

When using ion-irradiation to simulate neutron irradiation it is necessary to be able to calculate the number of ions needed, per unit area irradiated, to create a certain number of displacements per atom (dpa). The required ion dose ( $\phi_{ions}$ ) is a function of three factors: the required number of dpa, the number of atoms being irradiated, and the number of atom displacements created by each ion.

$$\phi_{ions} = \frac{dpa \times \# \text{ of atoms}}{\text{Displacements per Ion}} \quad 2.2$$

The extent that high energy incident ions deflect and displace the atoms of the target substrate is assessed by computation. The most common software used for this is the SRIM (Stopping and Range of Ions in Materials) software [9, 20, 21, 23, 27].<sup>1</sup> SRIM is a collision approximation model that employs a Monte Carlo simulation to estimate probabilistic values for ion-atom interactions. It uses the Kinchin-Pease formula to estimate the number of atom knock-outs per incident ion [30].

The Kinchin-Pease model describes the probability of atom displacement resulting from collision of a PKA, of known energy, with lattice atoms of known binding energy [31]. The formula is based upon an application of the condition of conservation of energy during inter-atomic collision events. The solution to the equations describing this model is obtained iteratively and is a function of the energy lost to the lattice structure during the collision, the PKA energy, and the inter-atomic binding energy [31].

The SRIM software works by running thousands of ion-atom interaction simulations, each expressed in terms of the Kinchin-Pease model, and predicts the resulting ion path and atom-displacement events. From each simulated ion implantation, SRIM calculates the mean, and variance of the penetration depth and the number of ion-induced displacements (i.e. irradiation damage events) of the substrate atoms [30].

SRIM estimates the net atomic displacement created by each ion including primary, secondary, and tertiary atom knock-on events [17, 19, 28, 30]. SRIM thus estimates the interaction depth of the ions within the substrate atoms [30]. This provides the average stopping range of the ions. We can use the information provided by SRIM simulations to determine  $\phi_{ions}$  by expanding Equation 2.2 as

$$\phi_{ions} = \frac{dpa \times \rho \times N_A \times \text{Stopping Range}}{\text{Displacements per Ion} \times \bar{m}_a} \quad 2.3$$

---

<sup>1</sup> SRIM is freely available for download at <http://www.srim.org/SRIM/SRIMLEGL.htm>

where  $\rho$  is the density of the substrate material,  $N_A$  is Avogadro's number, and  $\overline{m}_a$  is the average atomic mass of the substrate material, which can be calculated given the elemental composition of the material.

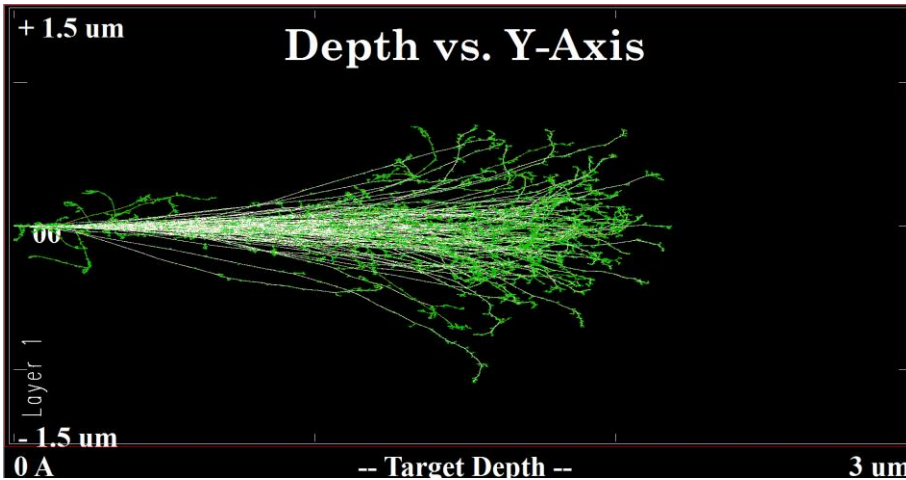


**Figure 2.12 Dislocations of 8.0 MeV Fe ions irradiating pure Fe. This shows the dislocations and cascade dislocations of 100 simulated ions.**

### 2.2.3 Effect of neutron/ion irradiation on material properties

During particle (ion or neutron) irradiation, crystallographic damage arises and this reduces ductility and increases the hardness of the exposed material (Figures 2.9, 2.10) [9, 20, 21, 32]. The fundamental ion-atom displacement event is referred to as a “Frenkel pair” and accounts for the majority of the crystal damage occurring during ion or neutron irradiation. Frenkel pairs are the displacement of a lattice atom to an interstitial site resulting in the creation of both an interstitial atom and a vacancy (Figure 2.7d). Both the vacancy and the interstitial point defects are highly mobile especially when the temperature is elevated [32].

When the interstitial and vacancy defects move there is a very high probability for recombination (i.e. the interstitial atom dropping into the vacancy site). In this case the point defect has been removed and the material “recovers” to its non-defected state. Similar

recombination can occur when point defects move to free surfaces or internal interfaces such as grain boundaries and interface boundaries.

Dislocation loops are another result of point defect movement. Vacancies and interstitials are very mobile along close packed atomic planes (CPP). As either vacancies or interstitials gather together in a plane, it becomes energetically favourable to form discs whose edges essentially define a planar dislocation loop. Dislocation loops are very hard to move and, relative to point defects, and thus more resistant to thermal recovery (Figure 2.13). Figure 2.8 is a collection of TEM images, showing the development of dislocation loops in a Zr foil from  $\text{Kr}^{2+}$  ion irradiation.

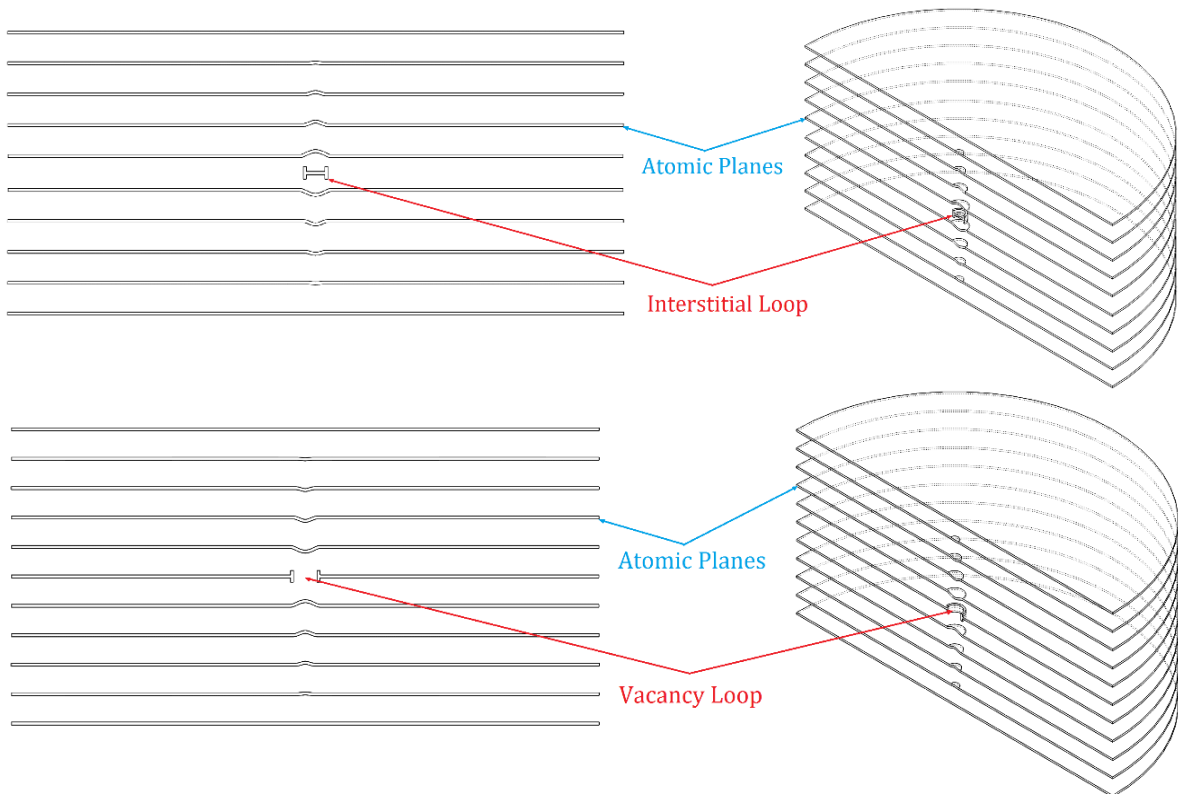


**Figure 2.13 Interstitial and vacancy dislocation loops. The anisotropic stress on adjacent atomic planes causes a warp in the local lattice structure, increasing the energy required for dislocation and defect glide through the material to occur.**

Volumetric defects are a common concern in neutron irradiation studies. Volumetric defects often arise in nuclear materials due to several phenomena:

1. irradiation-induced dissolution of second-phase precipitates
2. irradiation-induced clustering of alloy/impurity elements
3. generation of small H and He filled cavities within an alloy due to the radioactive decay of unstable isotopes generated by a fission process [10, 33 - 36].

#### 2.2.4 Neutron and ion irradiation summary

In summary, neutron and ion irradiation generally harden crystalline metals [15 - 18]. When high energy particles bombard a crystalline material the atoms are displaced and form vacancy and interstitial defects in the form of Frenkel pairs [19 - 21]. These point defects are quite mobile and either annihilate by recombination or cluster to form dislocation loops or other dislocation-type structures [19]. Compared to point defects, dislocation loops are difficult to move and are the primary contribution to the commonly observed increase in hardness of materials when they are exposed to neutron/ion irradiation. The recovery of irradiation damage is therefore a diffusion based problem therefore is highly dependent upon temperature.

### 2.3 Thermally-activated recovery of irradiation damage

As described in Section 2.2, irradiation hardening of nuclear materials occurs primarily by generation of simple point defects and dislocation loops within the material. These defects impede the motion of dislocations during plastic deformation and thus cause an increase in the material's yield stress. Recovery is the removal of these defects through recombination by the diffusion mechanisms illustrated in Figure 2.14.

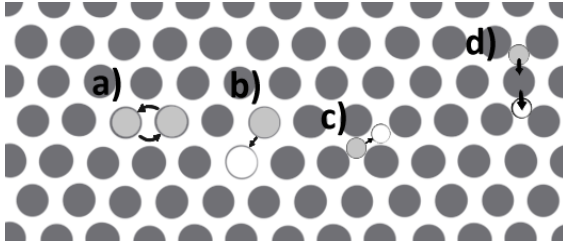


**Figure 2.14 Four simple mechanisms by which atoms can move in a crystalline material a) the ring mechanism b) the vacancy mechanism c) the interstitial mechanism d) the interstitialcy mechanism.**

The motion of small defects during heating can be described by the statistical motion (i.e. the jump frequency) of individual atoms in a crystal. It is this jump frequency that describes the rate of recovery of the irradiation damage. It is the primary objective of this thesis to determine the rate of recovery of irradiation hardening of two candidate alloys proposed for use as fuel cladding and pressure tube liners in Canada's Gen IV SCWR. The conventional model used to express the temperature dependence of the atomic jump frequency is described below. This model that will be applied in subsequent chapters of this thesis to express the rate of thermal recovery of irradiation induced hardening.

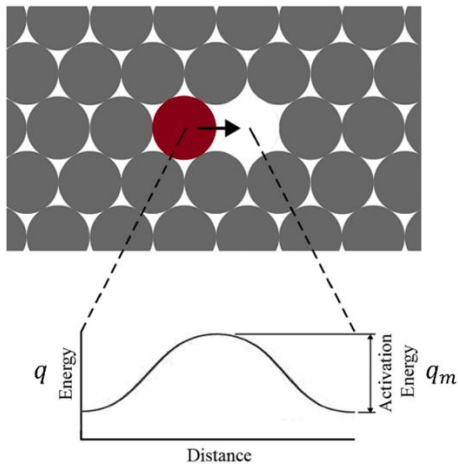


**Figure 2.15 Illustration of the energy,  $q$ , required for an atom to move towards an adjoining vacancy. If the thermal vibration energy  $\geq q_m$  an atom can move into the vacancy.**



For an atom to move by one atomic position it requires more energy,  $q$ , than the activation energy,  $q_m$ , of the particular diffusion mechanism (Figure 2.15) [37]. For recovery to occur, a material's temperature is increased to raise the average kinetic energy of the atoms such that their total internal energy

$$q_T = q_{kin} + q_o \quad 2.4$$

approaches  $q_m$  [37]. The average  $\langle q \rangle$  of the atoms in a solid is described by Equation 2.5, where  $k_B$  is the Boltzmann constant ( $1.38 \times 10^{-23}$  J/atoms·K), and  $T$  is the absolute temperature [37].

$$\langle q \rangle = k_B T \quad 2.5$$

At any instant, not all atoms will have an energy of  $\langle q \rangle$ ; some atoms will have more and some will have less energy. The probability,  $p$ , of an atom having an energy greater than a certain value ( $q$ ) is expressed by Equation 2.6 below [37].

$$p = e^{-\left(\frac{q}{k_B T}\right)} \quad 2.6$$

Therefore, the probability that an atom has sufficient energy to move one atom space within a crystal is given as

$$p_m = e^{-\left(\frac{q_m}{k_B T}\right)} \quad 2.7$$

The actual process of atomic diffusion requires that the following two conditions be met:

- i. The atom must sufficient energy to move from its crystal location (i.e.  $q_T \geq q_m$ ).
- ii. The atom must have a vacancy next to it into which it can move (Figure 2.15).

Since a vacancy has a characteristic “formation” energy,  $q_v$ , an equation of the same “Maxwell-Boltzmann” form as Equation 2.6 will express the probability that a vacancy will be located in a specific lattice site in a crystalline material. The probability,  $p$ , that an atom will move into an adjoining vacancy is therefore the product of the probabilities corresponding to Conditions i and ii as

$$p = p_v p_m = e^{-\left(\frac{q_v + q_m}{k_B T}\right)} \quad 2.8$$

The atom jump frequency is then expressed as

$$v = v_0 e^{-\frac{q_v + q_m}{k_B T}} \quad 2.9$$

where the constant  $v_0$  is related to the characteristic frequency of atomic vibration (i.e. the Debye frequency) of the crystalline material [38]. This is an important concept related to the study of this thesis, since it describes the simplest mechanism by which irradiation-induced crystal defects can be recovered at elevated temperature. While thermal recovery in general has been well studied and understood for common alloys, thermal recovery of irradiation-induced crystal damage has been studied very little and is practically unstudied for Fe- and Ni-bearing alloys at the high temperatures envisioned for the Gen IV SCWR.

## 2.4 Measuring the rate of thermal recovery of mechanical properties

### 2.4.1 Stress relaxation testing

Many experiments have studied thermal recovery, and always find the rate of isothermal recovery of a crystalline material's properties will decrease with time [39]. This can be seen by the isothermal recovery of single crystal zinc plastically deformed at 223 K (Figure 2.16), which shows the change in hardness,  $\Delta H$ , fits an equation of the form

$$\Delta H = H_0 e^{-\alpha t} \quad 2.10$$

where  $H_0$  is the initial hardness,  $\alpha$  is a material specific constant, and  $t$  is the amount of recovery time.

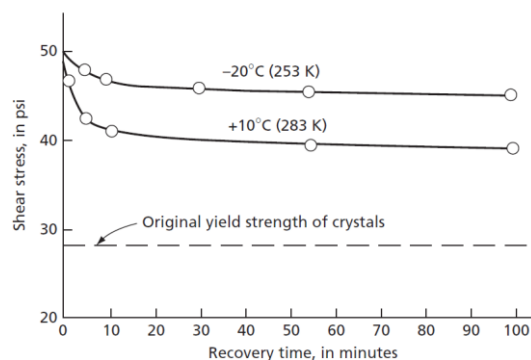


**Figure 2.16 Recovery of the yield strength of single crystal zinc at 253 K and 283 K [39]**

This also shows temperature can impact recovery, and suggests  $\Delta H$  can actually be modelled as

$$\Delta H = H_o e^{-\frac{\alpha t}{T}} \quad 2.11$$

where  $T$  is the recovery temperature. A recovery rate dependant both temperature and recovery time has not yet been characterized for irradiation hardened metals, however this thesis will study a temperature and time dependant recovery rate for AISI 310 and Inconel 800H.

To study relaxation rates, the experiment needs to be capable of measuring a material property, ideally with a high precision and grain-to-grain resolution, but also to isothermally heat a sample for very precise amounts of time in an environment which will not contaminate the surface.

#### 2.4.2 Micro-mechanical indentation testing

Micro-mechanical indentation hardness testing is a technique in which local mechanical properties are measured at nano-meter spatial resolution. Micro-indentation testing is capable of measuring grain-to-grain variations in hardness and also hardness of interfacial regions of polycrystalline materials. This technique is therefore ideal for the purpose of this thesis; i.e. the measurement of the effect of ion irradiation and thermal recovery on the mechanical properties of a region of metal that extends only several micrometers below the free surface of the test sample. These tests track force and indentation depth are recorded.

A micro-indentation hardness test first involves pressing a sharp-tipped, pyramidal shaped indenter into the test material a certain depth. The test ends by reducing the indentation force allowing the sample to elastically push the indenter; this distance is the elastic indentation depth,  $h_e$ . These tests usually include partial unloadings during the indentation cycle. Through testing of the force-depth data at an unloading, the plastic depth,  $h_p$ , has been approximated as

$$h_p = h_t - \frac{h_e}{2} \quad 2.12$$

where  $h_e$  is the elastic depth and  $h_t$  is loaded depth (Figure 2.17) [40].

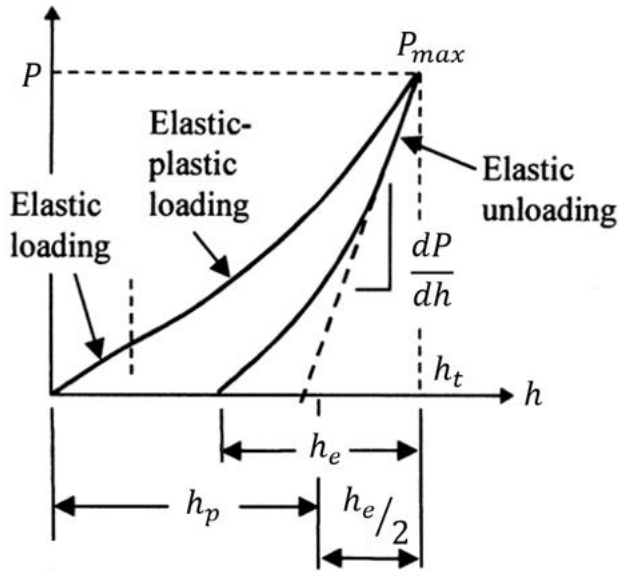


**Figure 2.17 Indentation force,  $P$ , versus indentation depth,  $h$ , for an elastic-plastic specimen [40]**

The area,  $A_p$ , of the indentation, projected normal to the indentation direction, can be calculated from  $h_p$ , which for a perfect three-sided pyramidal “Berkovich” indenter, is given as

$$A_p = 24.5h_p^2 \quad 2.13$$

The area function of an “actual” indenter will inevitably be affected by a certain amount of indenter tip rounding causing  $A_p$  to typically be expressed by a higher order function of  $h_p$ . In this case  $A_p(h_p)$  is determined experimentally by performing indentations on a standard of well-known hardness, such as quartz or sapphire. The area function in conjunction with the force allows the indentation hardness,  $H$ , to be calculated as

$$H = \frac{P}{A_p(h_p)} \cong \frac{P}{24.5h_p^2} \quad 2.14$$

Considerable study has been made upon the relationship between  $H$  and the yield stress,  $\sigma_y$ , of the indented material. Tabor reported that the hardness of the majority of common

metals was approximately  $3\sigma_y$  and subsequent more detailed studies of specific alloy systems have shown that this relationship holds surprisingly well for the vast majority of ductile metals [41, 42].

During micro-indentation hardness studies, it is important to realize that the volume of the sample that is plastically deforming, and hence contributing to the calculated hardness value, extends significantly deeper than the actual indentation. This makes it critical to be able to determine the actual depth of the plastic zone beneath the indenter. K. L. Johnson analysed the size of the plastic zone beneath an axisymmetric conical indentation made in an isotropic non-hardening material and determined that the plastic zone radius,  $c$ , was related to the indentation width,  $a$ , as

$$\frac{c}{a} = \left[ \frac{E_R \tan \alpha}{6\sigma_y(1-\nu)} + \frac{2}{3} \left( \frac{1-2\nu}{1-\nu} \right) \right]^{1/3} \quad 2.15$$

where  $\nu$  is the Poisson's ratio,  $\sigma_y$  is the yield stress,  $E_R$  is the reduced elastic modulus, and  $\alpha$  is the apex angle of the indenter (Figure 2.18) [43].  $E_R$  is the combination of the elastic moduli of the indenter head and the sample and is determined by

$$\frac{1}{E_R} = \frac{(1-\nu^2)}{E} + \frac{(1-\nu'^2)}{E'} \quad 2.16$$

where a primed term applies to the indenter tip as opposed to the test sample. [42]

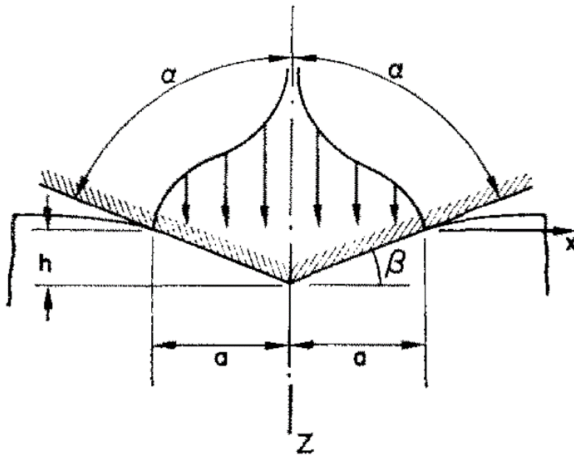


**Figure 2.18 Geometry of an axisymmetric conical indentation used by Johnson to calculate the relationship between the indentation plastic zone radius “ $c$ ” and the indentation width “ $a$ ” (Equation 2.15) [43].**

In the case of a Berkovich indenter, Equation 2.13 can be rearranged to express  $c$  as

$$c = \frac{h}{\tan(\beta)} \left[ \frac{E_R \tan \alpha}{6\sigma_y(1-\nu)} + \frac{2}{3} \left( \frac{1-2\nu}{1-\nu} \right) \right]^{1/3} \quad 2.17$$

where  $h$  represents the indentation depth,  $\beta$  represents the angle between the indentation direction and the sample surface ( $\beta = 90^\circ - \alpha$ ), which for a Berkovich indenter is approximately  $32^\circ$ .

Substituting values representative of our test material and indenter into Equation 2.15, we found

$$c \approx 11.5h \quad 2.18$$

using  $\beta = 20^\circ$ ,  $\nu = 0.36$ ,  $E_R = 184$  GPa, and  $\sigma_{y \text{ irradiated}} \cong \frac{H_{\text{irrad}}}{3} \cong 1.33$  GPa [44], where  $H_{\text{irrad}} \cong 4.0$  GPa. This means the radius  $c$  of the plastic zone is about 1.15, 2.31, and 4.61  $\mu\text{m}$  for indentation depths of 100, 200, and 400 nm respectively. Equation 2.18 is very close to the  $c = 12h$  calculated by elastic-plastic finite element analyses, for pyramidal indentations of the same geometry as that used in this study [45, 46].

### 2.4.3 Depth dependence of micro-indentation hardness

Indentation hardness is well known to be strongly affected by indentation depth [47 - 49]. When the indentation depth is very shallow, typically less than several micrometers, the measured hardness of most crystalline materials is significantly higher (Figure 2.19) [47 - 49].

Indentation size effects in crystalline materials

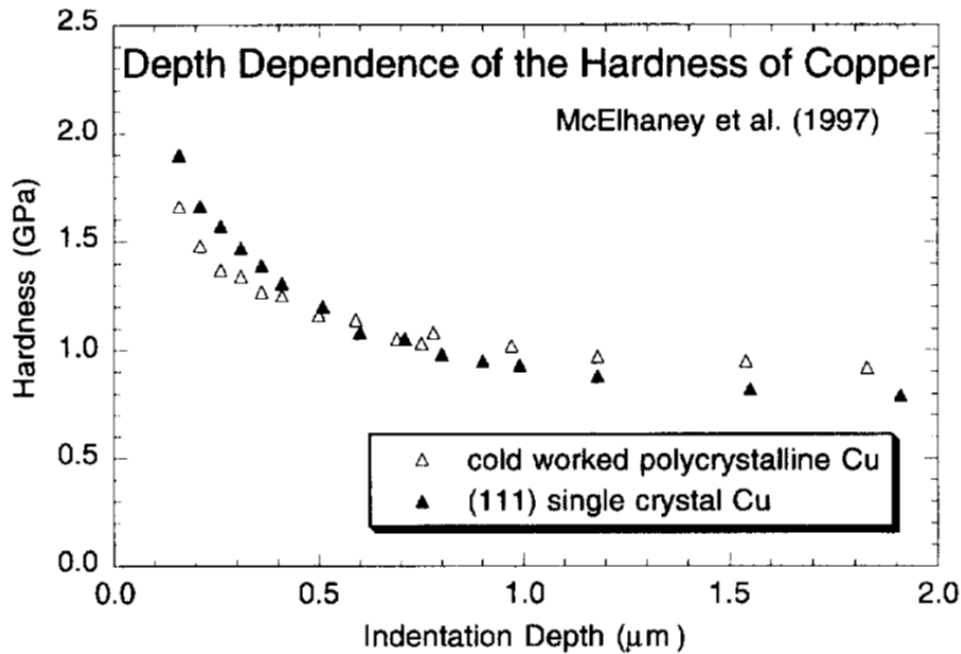


**Figure 2.19 Evidence of depth dependence of the hardness of single crystal and cold worked, polycrystalline Cu using micro-indentation with a diamond Berkovich indenter [49].**

This observation has been interpreted in terms of the fact that small indentations require a larger dislocation density around them to accommodate the required shape changes associated with the indentation process. *Stelmashenko et al.* proposed that during small indentations extra “geometrically necessary” dislocations must be created alongside the “statistically stored” dislocations that are necessary for all indentations regardless of depth [50]. This increased dislocation density translates to an increased yield stress and, hence, an increased hardness.

Further analysis of this finding by *Nix and Gao* demonstrated that, for common ductile metals, a linear relationship exists between the square of the measured hardness,  $H^2$ , and the reciprocal of indentation depth,  $1/h$ , (Figure 2.20) [48].

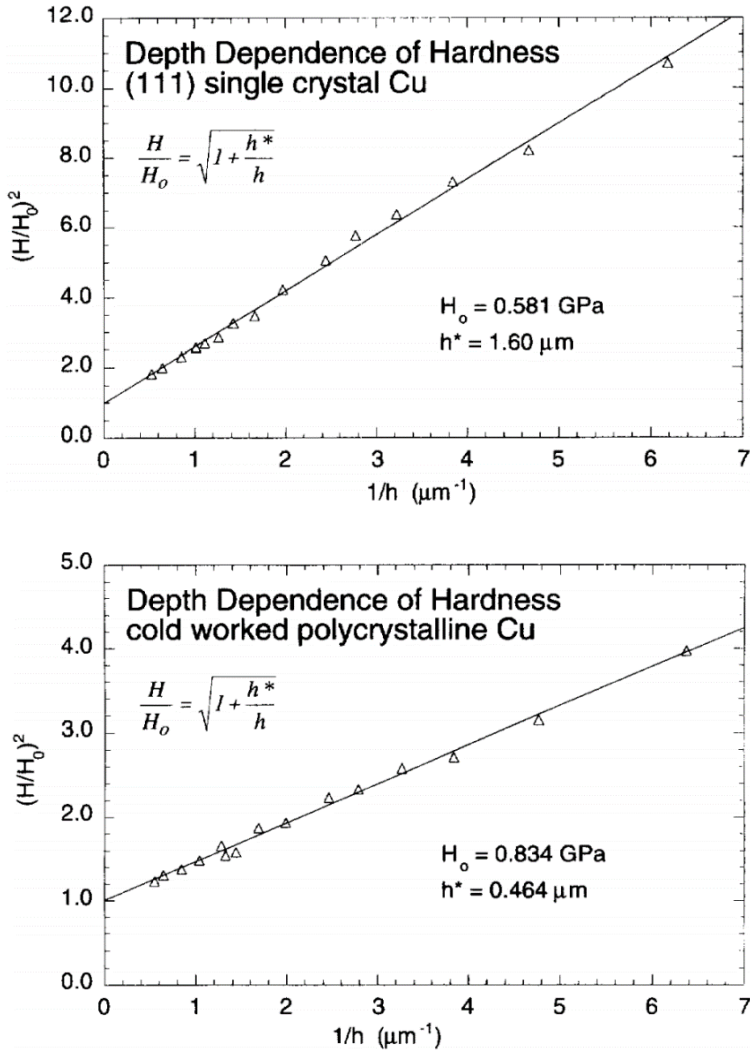


Figure 2.20 McElhaney's data from Figure 2.19 replotted by Nix and Gao [48].

This linearity is expressed as

$$\frac{H}{H_0} = \sqrt{1 + \frac{h^*}{h}} \quad 2.19$$

where  $H_0$  is the bulk hardness and  $h^*$  is a length indicative of the depth dependence of  $H$  [48]. The  $H_0$  and  $h^*$  can be found through *Stelmashenko's* analysis as

$$H_0 = 3\sqrt{3}\alpha\mu b\sqrt{\rho_s} \quad 2.20$$



$$h^* = \frac{81}{2} b \alpha^2 \tan^2 \theta \left( \frac{\mu}{H_o} \right)^2 \quad 2.21$$

where  $\alpha$  is a constant set to 0.5,  $\mu$  is the shear modulus,  $b$  is the magnitude of the Burgers vector,  $\rho_s$  is the statistically stored dislocation density, and  $\theta$  is the contact angle between the indenter and the material being tested [48]. Thus,  $H_o$  and  $h^*$  are dependent entirely on the properties of the test material and the indenter, but not the indentation depth.

It is crucial that indentation depth be acknowledged during data analysis. In this study we will use the theory described above to assess the indentation depth dependence of the hardness of the AISI 310 and the Inconel 800H alloys.

## 2.5 Summary

In this chapter, relevant background information on the: i) general layout and operation of the proposed Canadian Gen. IV SCWR core, ii) characteristics of the neutron/ion induced crystallographic damage, iii) mechanisms by which simple crystal defects, such as point defects (Frenkel pairs) and small dislocation loops can be recovered by atom diffusion, and iv) micro-indentation hardness test technique for measuring local mechanical properties of materials was provided.

Noteworthy points raised in this chapter which have relate to the data presented in the remainder of this thesis are:

- The fuel cladding and pressure tube liner of the proposed Canadian Gen. IV SCWR will be exposed to the highest temperatures of the reactor core, up to about 800°C, and obviously must not fail at these temperatures.
- High energy self-similar heavy ion irradiation induces irradiation damage to the target material that is very similar to the damage induced by fast neutron irradiation while in a nuclear reactor core.
- The advantages of using ion irradiation include: i) very fast damage rates, and ii) irradiated samples are not radioactive

- The major disadvantage of ion irradiation is that the resulting crystallographic damage exists in a very small region that is only several micrometers in thickness beneath the irradiated surface.
- The ion irradiation dosage necessary to impart a specific amount of irradiation damage can be calculated with the use of Equation 2.3 and SRIM ion-atom interaction software.
- Defects cause the observed irradiation hardening by acting as uniformly distributed simple obstacles that impede plastic deformation by dislocation glide.
- Since the defect structure resulting from ion irradiation is very simple, its rate of recovery at elevated temperature can be expressed by a very simple model based upon the statistical probability that an atom will jump to a neighboring lattice site (Equation 2.8).

Micro-indentation hardness testing is a suitable method to test the effect of ion irradiation and recovery temperature/time on the hardness of small, micrometer size, regions of a sample. This technique will therefore be used for this thesis research.

## Chapter 3

### 3 Experimental Procedure

#### 3.1 Sample preparation

The study undertaken in this thesis was performed on two alloys; AISI 310 and Inconel 800H (Table 3.1). These alloys were identified by the Canadian Gen IV review committee as leading candidate alloys for the fuel cladding and the pressure tube liner components.

**Table 3.1: Chemical composition, in weight percentage, of the Inconel 800H and AISI 310 alloys [11, 12]**

	<b>C</b>	<b>Al</b>	<b>Si</b>	<b>P</b>	<b>S</b>	<b>Ti</b>	<b>Cr</b>	<b>Mn</b>	<b>Fe</b>	<b>Ni</b>	<b>Cu</b>	<b>Mo</b>
<b>AISI 310</b>	0.08	-	0.75	0.05	0.03	-	<b>25.00</b>	2.00	<b>50.34</b>	<b>20.50</b>	0.50	0.75
<b>800H</b>	0.08	1.40	1.00	0.05	0.02	1.40	<b>21.00</b>	1.50	<b>39.80</b>	<b>33.00</b>	0.75	-

The AISI 310 alloy is an austenitic stainless steel consisting of equiaxed, FCC grains typically from 10 microns to 100 microns in diameter. The alloy contains 25 weight percent chromium to maintain a passive corrosion resistant chromium oxide surface layer. This alloy has a maximum service temperature of 1090° C and is frequently used for flare tips, radiant tubes, burners and combustion chambers, food processing equipment [12].

The Inconel 800H alloy is a ferrous based super alloy that consists of equiaxed, FCC grains typically from 50 microns to 1400 microns in diameter. The higher nickel content in this alloy relative to the AISI 310 alloy provides superior corrosion and creep resistance at elevated temperature by stabilizing the austenitic phase over high service temperatures. This alloy has a maximum service temperature of 790° C and is frequently used for heat exchangers, pressure vessels, and dampers [11].

The AISI 310 and Inconel 800H materials were acquired in the form of ½” thick bar stock from Rolled Alloys Inc. (rolledalloys.ca). Small samples of approximately 13 mm × 13 mm × 1 mm were cut from the bars using wire electric discharge machining.

The small samples were then glued, using Loctite 454 adhesive, to metal blocks to facilitate handling during surface grinding/polishing. The mounted samples were ground smooth by hand using wet silica carbide abrasive paper. Grinding was started with 100 grit paper and proceeded with successively finer grits when surface roughness was minimized. The finest grinding was performed with 4000 grit paper.

The ground samples were then mechanically polished with a wool felt cloth in an aqueous suspension of alumina abrasive. Successive polishing steps started with 1  $\mu\text{m}$  alumina powder and ended with 50 nm alumina powder. Between each polish, the samples were thoroughly cleaned with distilled water.

Initial testing revealed that this type of mechanical polishing, involving successively finer polishing steps, did not remove all the plastically deformed material, caused by mechanical grinding, beneath the polished surface of the sample. This residual plastic deformation ultimately resulted in significant scatter in the measured micro-indentation hardness obtained when the tests were performed at indentation depths less than about 2  $\mu\text{m}$ . This variability was mitigated significantly through the following procedure.

First, the polished samples were cleaned and carefully placed in a metal annealing envelope, which was then filled with an inert gas and sealed. The sealed envelope was heated at 1000° C for 15 minutes to anneal out any residual cold work resulting from the previous grinding/polishing and then air cooled. The samples were then removed from the envelope and lightly polished, with an aqueous suspension of 50 nm alumina, to remove any oxidation resulting from the annealing step. Subsequent micro-indentation hardness testing displayed significantly less scatter in the indentation hardness.

The polished Inconel 800H and the AISI 310 samples were then chemically etched to identify the grain size and shape. Both alloys were etched by immersion in a 25% HCl, 25% HNO<sub>3</sub>, and 50% Glycerol solution. Optimal etching immersion time for the AISI 310 alloy was 145 seconds while the Inconel 800H alloy was 60 seconds. Once etched, the samples were immediately rinsed with distilled water and dried using compressed air. Figures 3.1 and 3.2 show the etched microstructure of each alloy.



**Figure 3.1 Microstructure of AISI 310 observed with an optical microscope.**

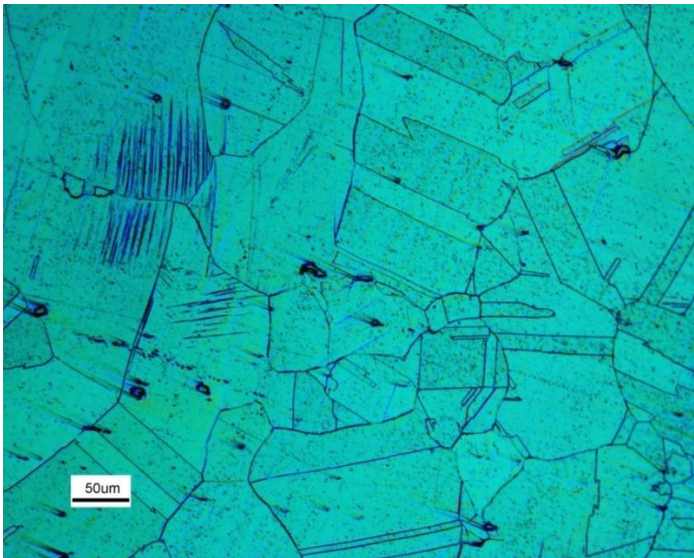


**Figure 3.2 Microstructure of Inconel 800H observed with an optical microscope.**

Both alloys are primarily single FCC phase and contain considerable twinning features. AISI 310 alloy has large grains which are typically between 10 and 100  $\mu\text{m}$  in diameter, while the grain size of Inconel 800H is between 100  $\mu\text{m}$  and 2 mm.

## 3.2 Ion Irradiation

High energy iron ion irradiation was used to simulate neutron irradiation as described in Section 2.2.1. Polished, but non-etched, samples of AISI 310 and Inconel 800H were exposed to 8.0 MeV  $\text{Fe}^{4+}$  ions at the Tandetron Accelerator Facility at the University of Western Ontario.

This ion accelerator operates by using cesium ions to sputter an iron target; creating low energy  $\text{Fe}^-$  ions [47]. The  $\text{Fe}^-$  ions are accelerated through a 1.6 MV magnetic field into a low pressure (approximately  $10^{-3}$  to  $10^{-4}$  Torr) nitrogen gas chamber, known as a stripper canal [48]. The nitrogen strips each  $\text{Fe}^-$  ion of 5 electrons creating a beam of  $\text{Fe}^{4+}$  ions. A 1.6 MV magnetic field then accelerates the beam of  $\text{Fe}^{4+}$  ions [48]. Therefore, the  $\text{Fe}^{4+}$  ions leaving the accelerator have a kinetic energy of

$$E_{\text{Fe}^{4+}} = \frac{1.6 \text{ MeV}}{\text{electron}} \times \frac{5 \text{ electrons}}{\text{ion}} = 8.0 \text{ MeV/ion} \quad 3.22$$

The ion beam is then focused, with an electromagnetic lens, to a diameter of approximately 2 mm and rastered over an aperture. The beam that passes the aperture then implants  $\text{Fe}^{4+}$  ions onto samples that are attached to an X-Y translation stage within the implantation chamber (Figure 3.3).

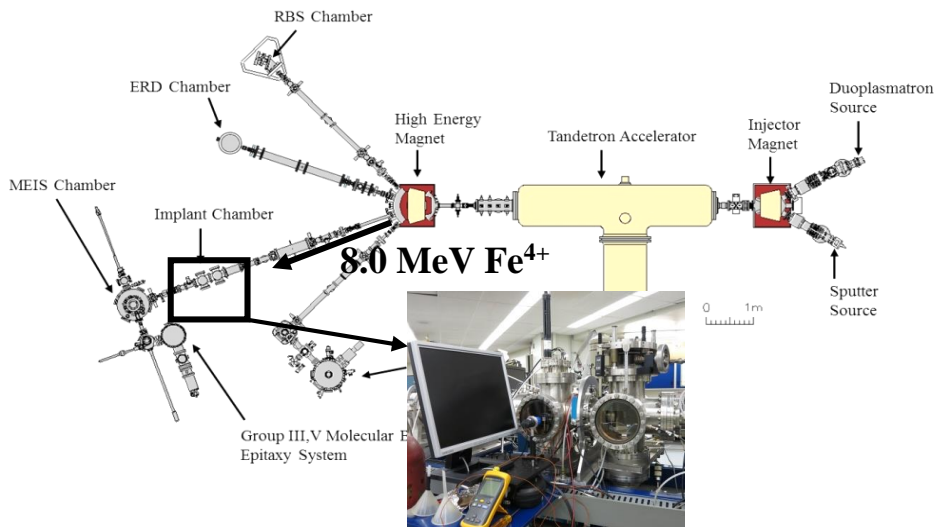


**Figure 3.3 Schematic illustration of the Tandetron ion accelerator located at the University of Western Ontario [49].**

The translational stage was used to move the sample with respect to the ion beam such that various regions of the sample were exposed to different, but well controlled, levels of Fe<sup>4+</sup> ion dosage (Table 3.2). For each level of ion dosage, the resulting irradiation damage (dpa) was calculated using Equation 2.3.

**Table 3.2: Test matrix for this study. The circles indicate tests performed on AISI 310 samples while the squares indicate tests performed on Inconel 800H samples.**

Irradiation damage (dpa)	As-irradiated	400°C anneal (minutes)				500°C anneal (minutes)				600°C anneal (minutes)		
		1	2	10	100	1	10	50	100	1	10	100
0	●, ■	●, ■	●, ■	●, ■	●, ■	●, ■	●, ■	●, ■	●, ■	●, ■	●, ■	●, ■
0.01	●, ■					●, ■	●, ■	●, ■	●, ■	●, ■	●, ■	●, ■
0.1	●, ■	●	●	●	●	●, ■	●, ■	●, ■	●, ■	●, ■	●, ■	●, ■
0.5	●	●	●	●	●							
1	●, ■	●	●	●	●	●, ■	●, ■	●, ■	●, ■	●, ■	●, ■	●, ■
2	●	●	●	●	●							
4	●	●	●	●	●							
8	●	●	●	●	●							
10	●, ■					●, ■	●, ■	●, ■	●, ■	●, ■	●, ■	●, ■
15	■	■	■	■	■							

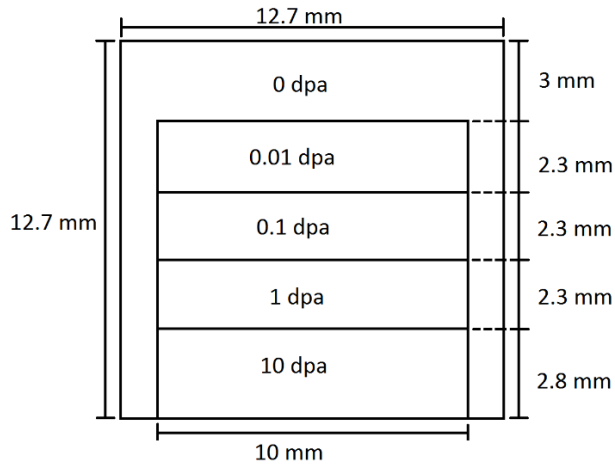


**Figure 3.4 Schematic illustration of typical regions of ion exposure for samples used in this experiment.**

### 3.3 Micro-indentation

The effect of ion irradiation and thermal annealing on the mechanical properties of the AISI 310 and the Inconel 800H alloys was assessed using micro-indentation hardness tests. The tests were performed with a NanoTest indentation machine (Micro Materials Ltd, Wrexham UK) equipped with a high-precision low-load (0.1 to 500 mN) indentation actuator and a diamond-tip Berkovich indenter (Figure 3.5). The indenter is held on a pendulum, which rotates freely about a pivot. The pendulum movement is controlled by an electromagnetic actuator consisting of a permanent magnet and a copper coil (solenoid). The indenter displacement is measured with a capacitance displacement gauge mounted behind the indenter. The nano-indenter records force with a precision of  $\pm 0.4$  mN and depth with a precision of  $\pm 0.4$  nm [50].

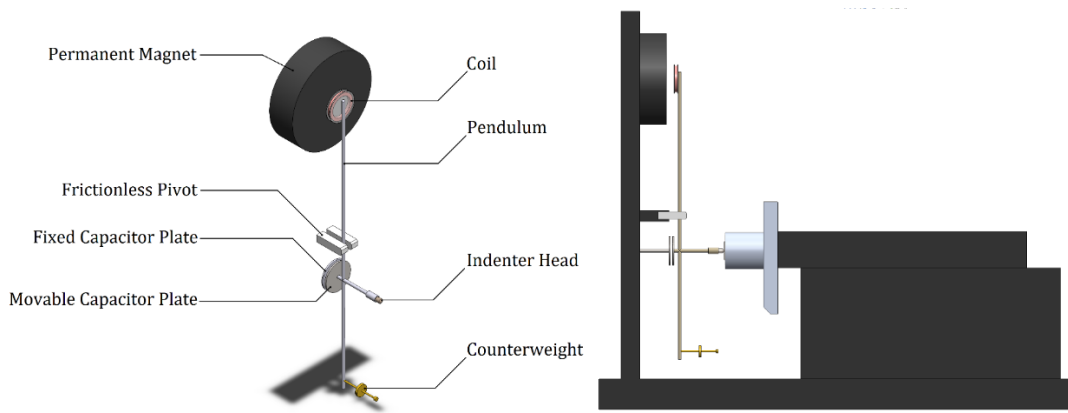


**Figure 3.5 Schematic illustration of the NanoTest indentation hardness testing platform that was used in this study.**

In this study, nine to eighteen indentation hardness tests were performed under each test condition listed in Table 3.2. Indentation tests were loaded using proportional loading to invoke a constant effective average indentation strain rate,  $\dot{\epsilon}$ , of 0.05/s [51]. This approach is based upon the well-established equation derived by *Haghshenas* [51] relating indentation load  $P$  and loading rate  $\frac{dP}{dt}$  to  $\dot{\epsilon}$ :

$$\frac{dP}{dt} \cdot \frac{1}{P} = \dot{\epsilon} \quad 3.2$$



Each indentation was performed to a maximum depth of 1.1  $\mu\text{m}$ . Periodic partial unloadings were performed every 100 nm indentation depth, starting at 200 nm. The indentation hardness,  $H$ , corresponding to each unloading point was calculated using Equations 2.10 – 2.12 and a polynomial indentation contact area function  $A(h_p)$  (Figure 3.6).

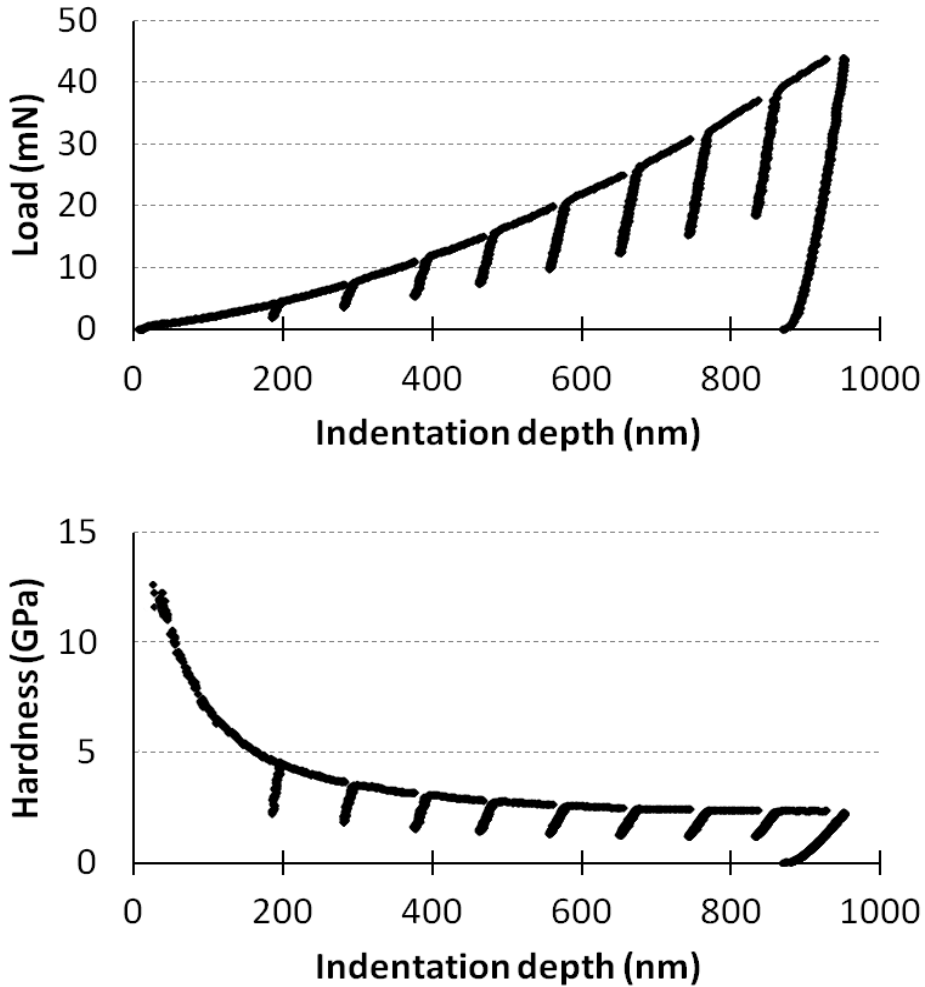


**Figure 3.6 Indentation force versus depth and corresponding indentation hardness,  $H = P/A$ , versus depth curves from a typical indentation test performed in this study. In this plot  $H$  is calculated from the *total* indentation depth. The partial unloading performed at indentation depth increments of 100 nm are shown. The slope of these unloadings are used to determine the plastic indentation depth  $h_p$  from which the actual hardness is calculated using Equations 2.10 - 2.12.**

$A(h_p)$  was determined for sub-micron indentation depths from a series of calibration indentations, with the same indenter, on a quartz test standard.<sup>2</sup> Each indentation was spaced at least 100  $\mu\text{m}$  apart to prevent overlap of the indentation affected regions.

Figure 3.7 shows a typical array of indentations made in one of the test samples.

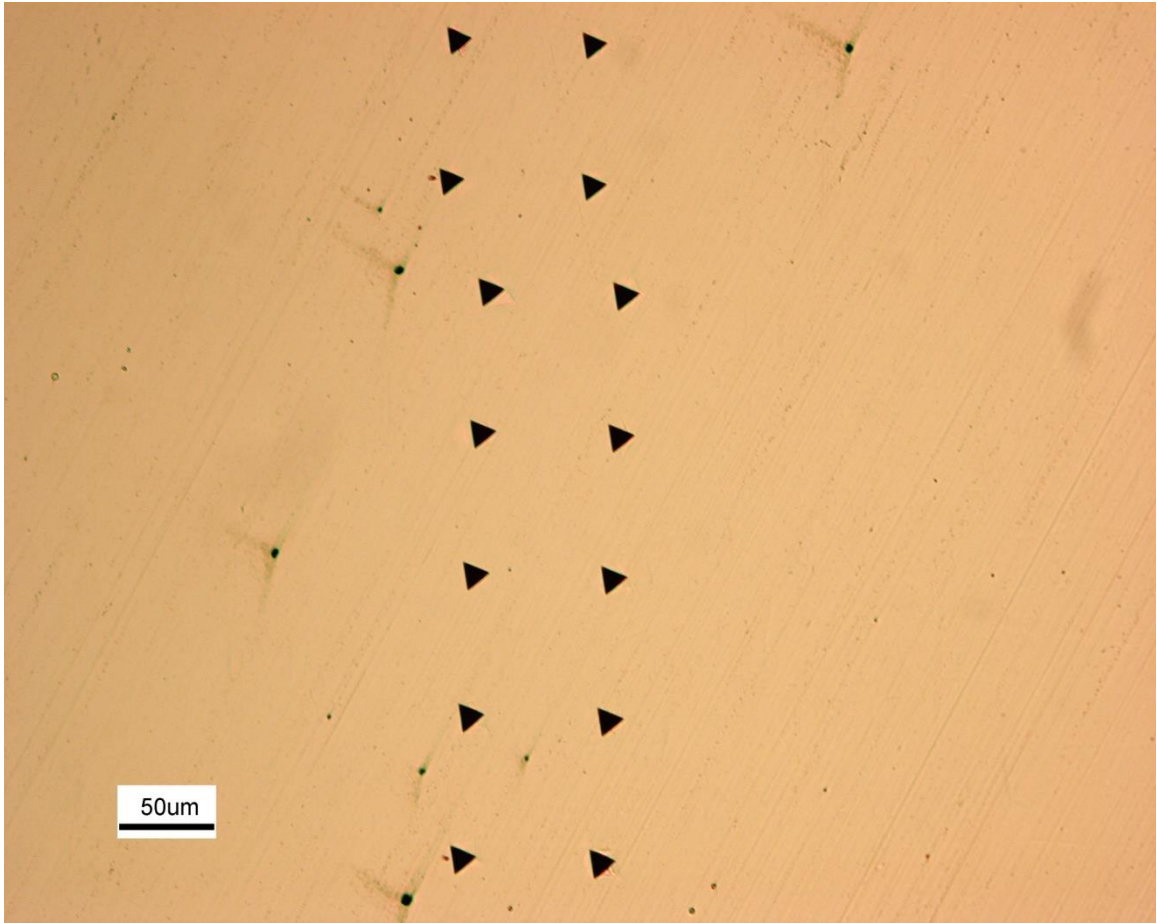


**Figure 3.7 Optical image of fourteen indentations from a  $7 \times 2$  indentation array.**

---

<sup>2</sup>  $A(h_p) = -1.980 \times 10^{-9}h_p^5 - 2.017 \times 10^{-6}h_p^4 + 0.00086h_p^3 + 23.844h_p^2 + 294.703h_p + 42715.743$  where the indentation depth,  $h_p$ , is in units of nm and less and indentation area,  $A(h_p)$  is in units of  $\text{nm}^2$ .

### 3.4 Thermal annealing

The rate at which the indentation hardness of the ion-irradiated samples decreased with heating was studied by placing the irradiated samples in a movable Vycor tube within an electrical resistance furnace. A positive pressure inert argon atmosphere was maintained in the tube. The furnace temperature was maintained at the test temperature (400, 500, or 600° C) with a precision of +/- 2° C. When the furnace temperature was established, the Vycor tube was moved such that the test samples were placed in the central hot zone of the furnace for the times specified in Table 3.2 (i.e. 1, 10, 100 minutes, etc.). The Vycor tube was then moved out of the furnace and the samples were allowed to cool to below 100° C while maintaining a low oxygen atmosphere. The annealed samples were then tested by indentation as described in Section 3.3.

## Chapter 4

### 4 Experimental Results

#### 4.1 Indentation hardness of the ion irradiated samples

Between nine and eighteen indentation tests were performed at each test condition listed in Table 3.2. A total of 3147 indentation tests were performed in this study. Each indentation test consisted of partial unloadings, usually 10, and from each one an indentation hardness value was calculated using the method described in Sections 2.4 and 3.3. Each indentation test therefore resulted in multiple values of  $H$  determined at different indentation depths.

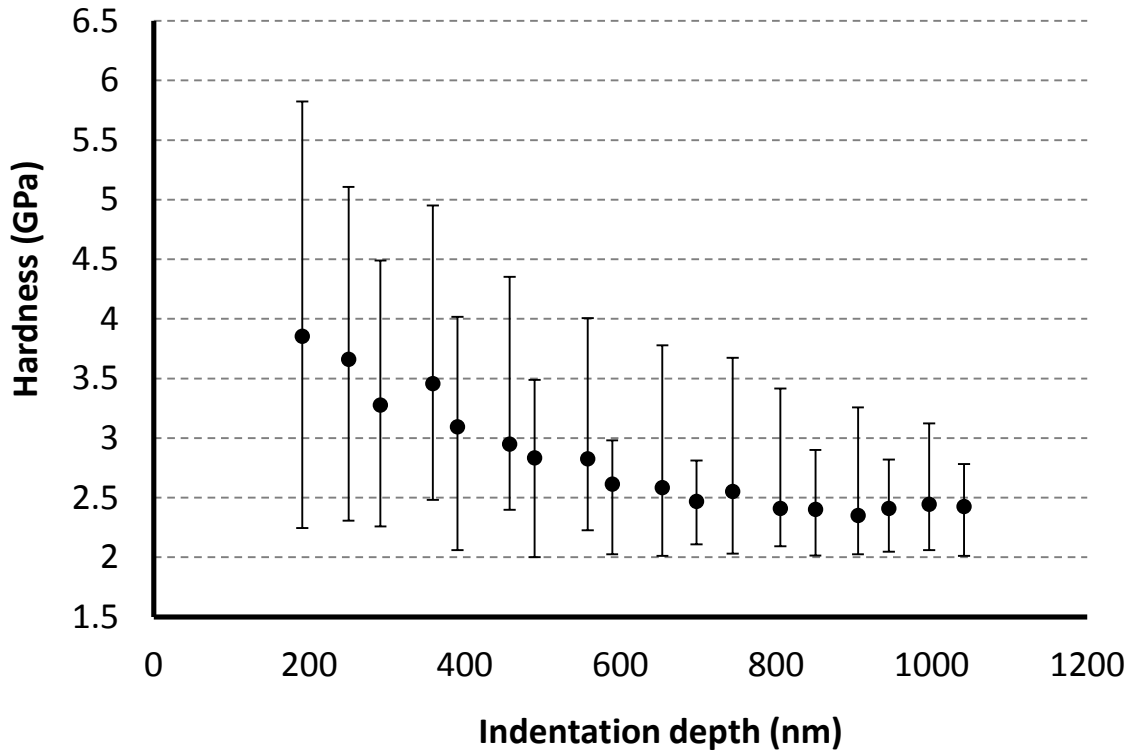


**Figure 4.1 Indentation hardness measured over a range of indentation depth for non-irradiated AISI 310.**

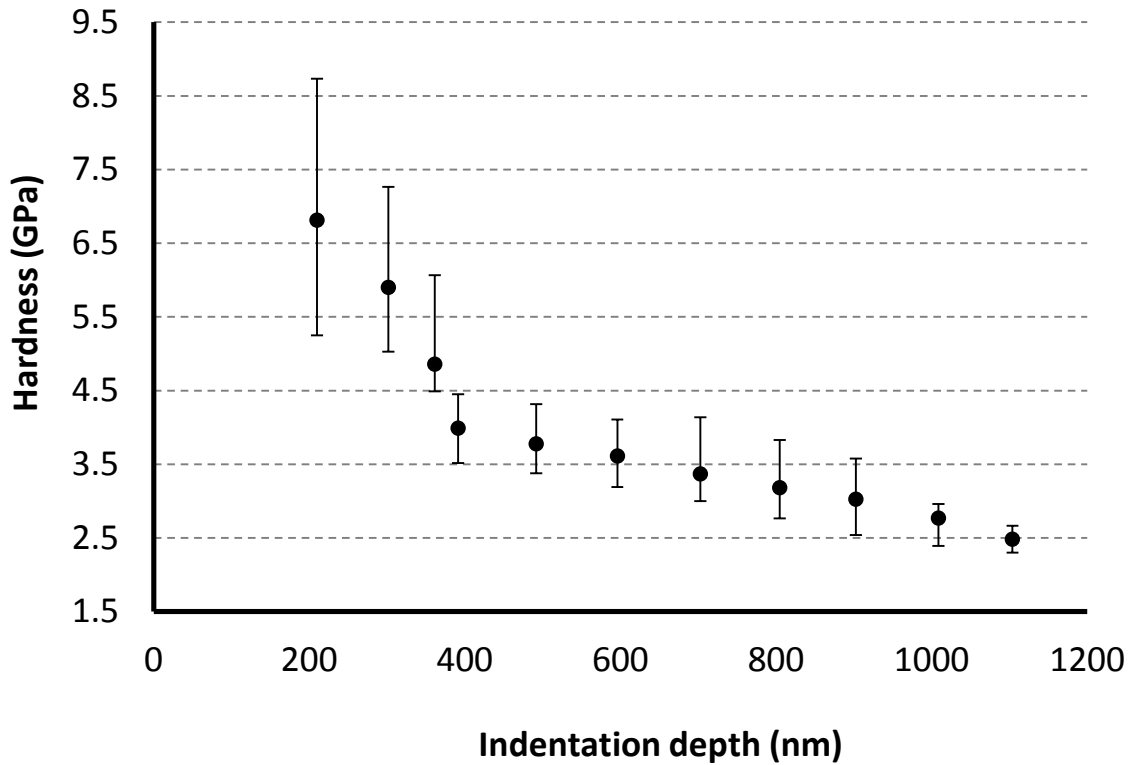


**Figure 4.2 Indentation hardness measured over a range of indentation depth for non-irradiated Inconel 800H.**

Figures 4.1 and 4.2 show the average  $H$  versus  $h$  for the non-irradiated AISI 310 and Inconel 800H material. The error bars shown on these plots indicate the indentation-to-indentation variation in the measured hardness for a given indentation depth. Both graphs indicate a clear indentation depth dependence of the measured hardness with the hardness being considerably larger at the small indentation depths. The depth dependence of  $H$  is a common observation for ductile metals and has been extensively studied and is attributed to the fact that the mechanisms of dislocation nucleation and glide become quite different in plastic zones around small indentations compared to those around large indentations. When the plastic zone is large, corresponding to that which is around a pyramidal indentation of depth larger than about  $5 \mu\text{m}$ , there are sufficient available close-packed

dislocation slip systems to accommodate the necessary shape changes imposed by the indentation process; thus, the hardness, and the corresponding yield stress, is low and is constant (insensitive to indentation depth for  $h \geq 5 \mu\text{m}$ ). When the indentation plastic zone is small, typical of indentations of depth less than about  $5 \mu\text{m}$ , the number of active close-packed slip systems is much reduced and may be unable to accommodate the required shape change. In this case dislocation nucleation and motion must occur on other, non-easy, slip systems and this requires higher stress and thus a higher hardness is measured [52].

## 4.2 Indentation hardness of the annealed samples

Figures 4.3 and 4.4 show the average  $H$  versus  $h$  for the ion-irradiated (non-heated) AISI 310 and Inconel 800H material. Once again, the error bars indicate the indentation-to-indentation variation in the measured hardness for a given indentation depth. As with the non-irradiated materials, the ion irradiated samples show hardness values that are clearly indentation depth dependent. A comparison of Figures 4.3 to 4.4 indicate that, for any indentation depth, the hardness increases with increasing ion irradiation damage (dpa). This clearly indicates the effect of ion-induced irradiation damage on the hardness of these alloys in the absence of thermal recovery. Further quantification of this irradiation hardening is performed in Chapter 5.

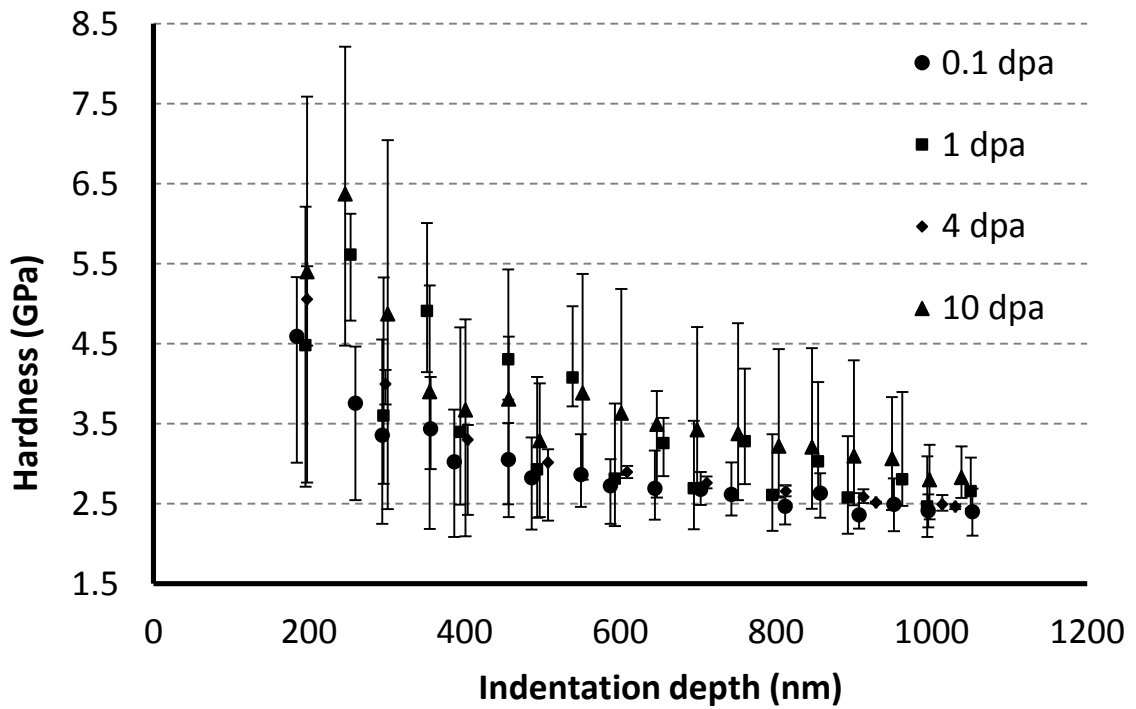
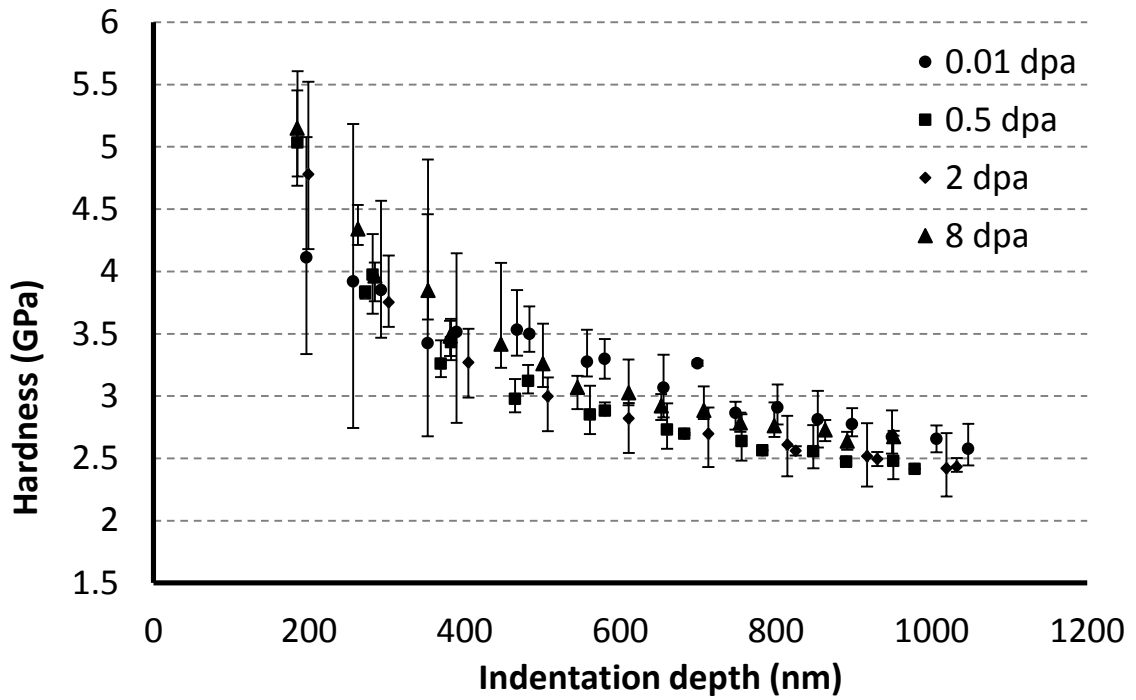


**Figure 4.3 Indentation hardness measured over a range of indentation depth for Fe<sup>4+</sup> irradiated AISI 310 samples before thermal recovery.**

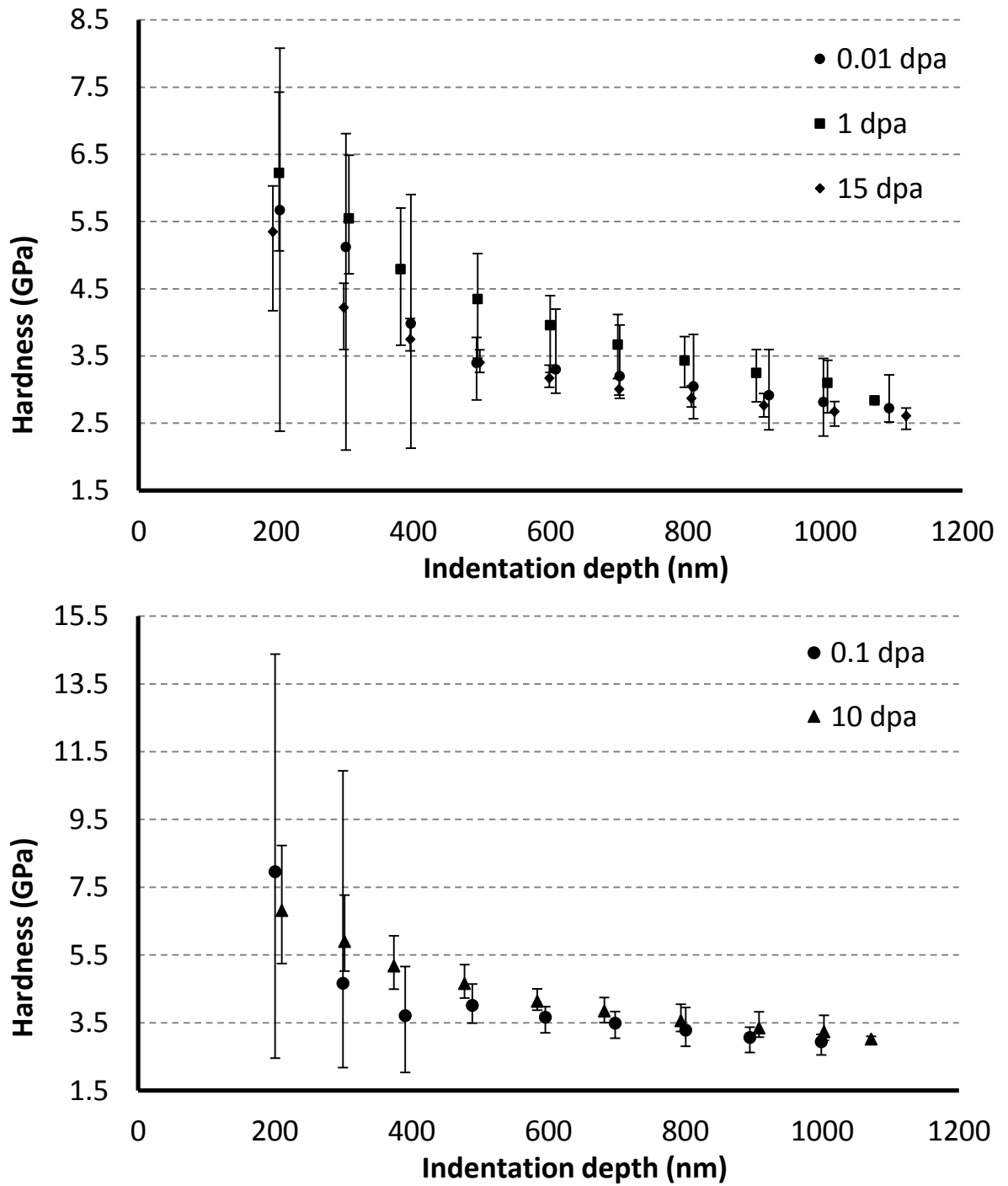
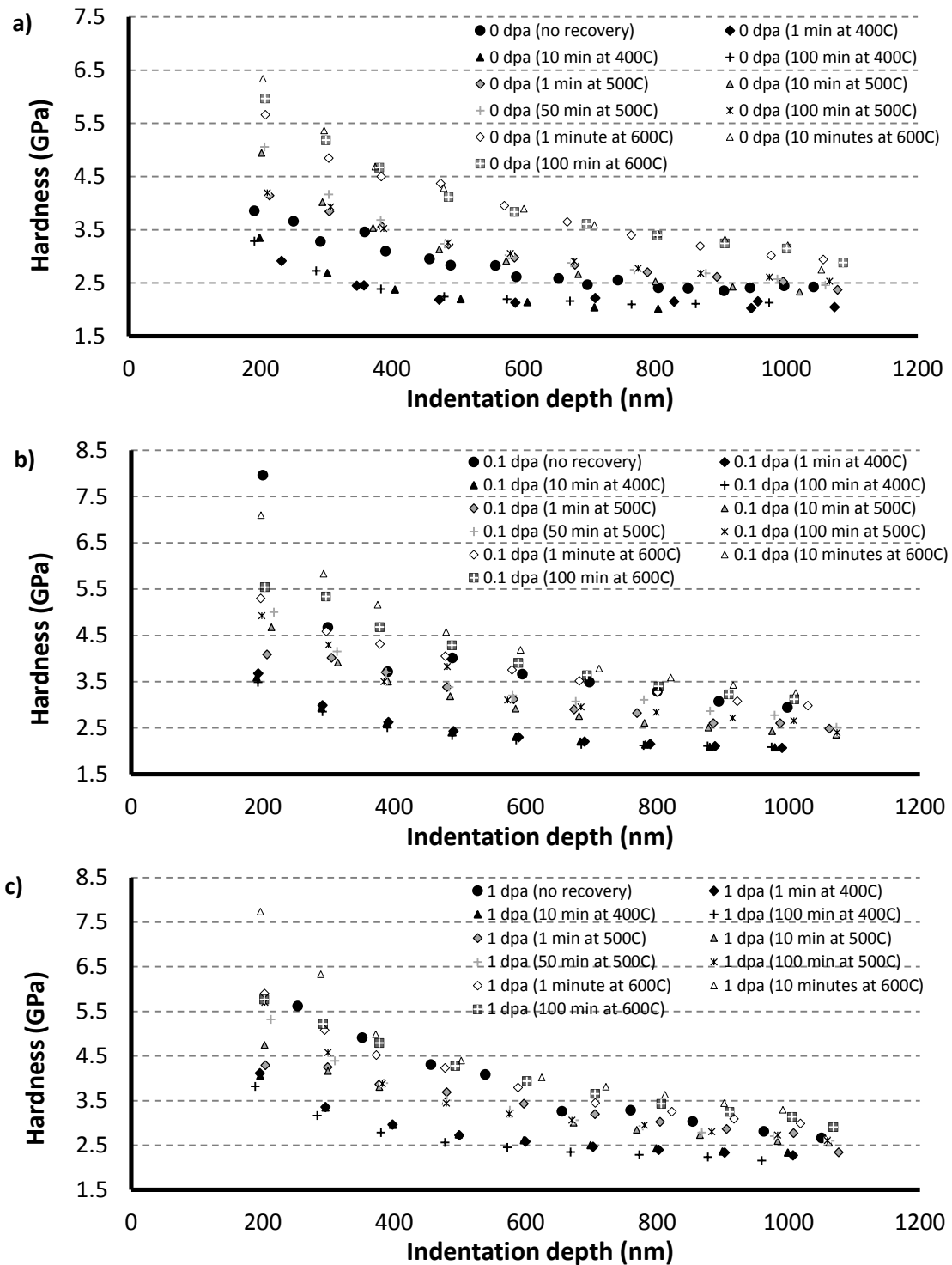
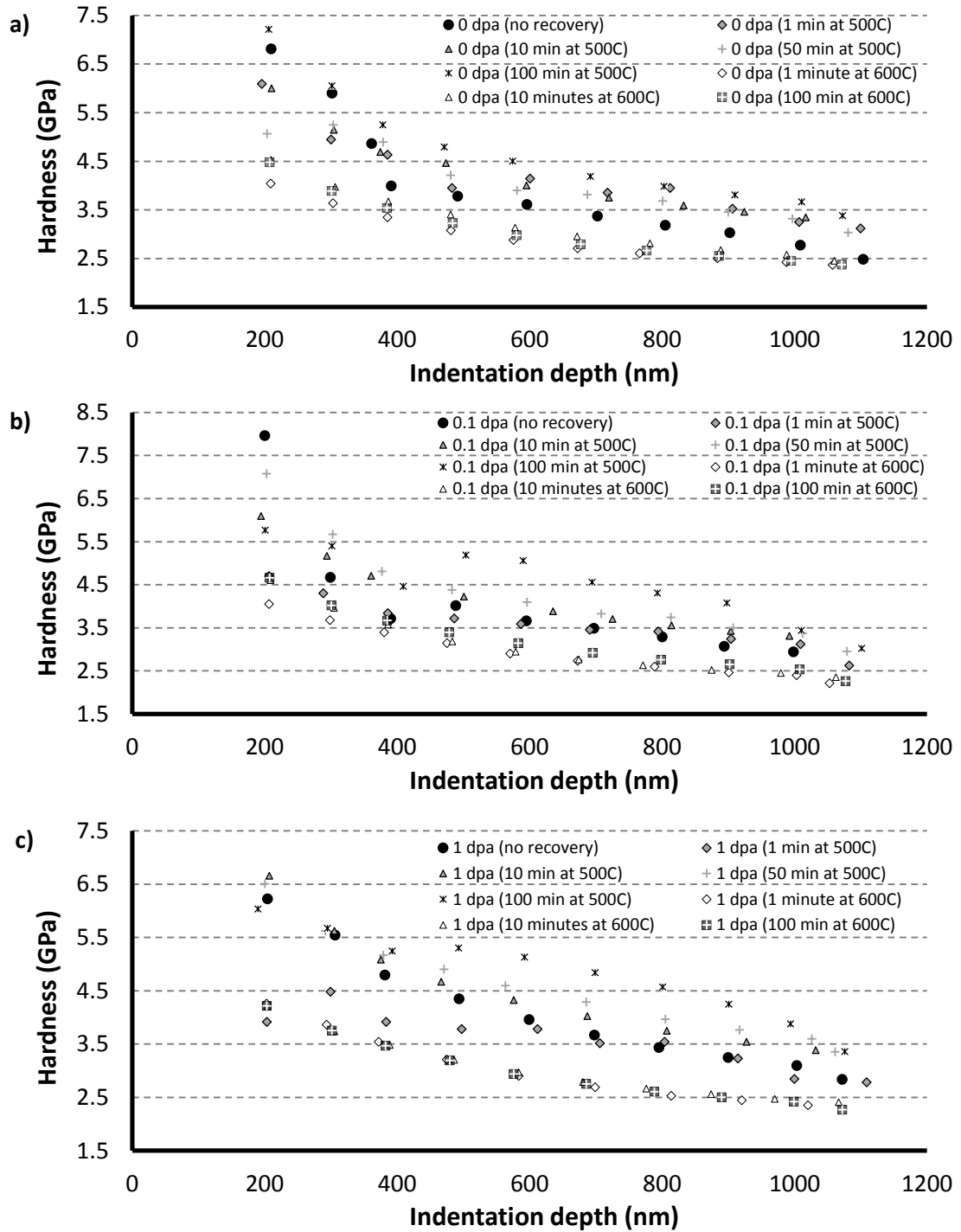


Figure 4.4 Indentation hardness measured over a range of indentation depth for Fe<sup>4+</sup> irradiated Inconel 800H before thermal recovery





**Figure 4.5 Indentation hardness measured over a range of indentation depth for samples that were annealed for various times and temperatures for: a) non-irradiated AISI 310; b) 0.1 dpa irradiated AISI 310; c) 1 dpa irradiated AISI 310.**



**Figure 4.6 Indentation hardness measured over a range of indentation depth for samples that were annealed for various times and temperatures for:**  
**a) non-irradiated Inconel 800H; b) 0.1 dpa irradiated Inconel 800H; c) 1 dpa irradiated Inconel 800H.**

Figures 4.5 and 4.6 show the average hardness versus indentation depth for the ion-irradiated AISI 310 and Inconel 800H samples that were annealed at 400° to 600° C for various periods of time. The figures indicate that the average hardness decreases with increasing indentation depth. The AISI 310 alloy recovers all irradiation hardening almost immediately upon annealing at 400° C. Annealing at 500° and 600° C, however, results in an apparent re-hardening of this alloy. Similarly, the Inconel 800H alloy softens during the first minute recovery at all annealing temperatures but quickly re-hardens when annealed at 500° and 600° C.

This suggests that the ion-induced point defects and small dislocation loops that cause the observed ion hardening are very rapidly removed when exposed to temperatures of 400° to 500° C. With extended exposure to temperatures above 500° C a hard surface oxide layer forms on both alloys resulting in an apparent increase in hardness. The rate that this oxide forms is alloy dependent with the Inconel 800H displaying more rapid oxide formation compared to the AISI 310 alloy. This observation is described below.

### 4.3 Oxidation during annealing

A potential issue with the experimental design was the formation of oxides on the surface of samples during the annealing stages of this study. Argon gas was passed through the annealing tube furnace, and then through a bubbler, for several hours prior to heating to remove any residual oxygen.

The 400° C samples that were heated for the longest duration, 1000 minutes, displayed visible surface discolouration, most notably on the Inconel 800H (Figure 4.7a). An interesting feature that was observed was that the intensity of the discolouration, indicative of increasing oxide thickness, was significantly lower in the regions of the samples that were exposed to ion irradiation: the higher the ion exposure the less surface oxidation occurred (Figure 4.7).

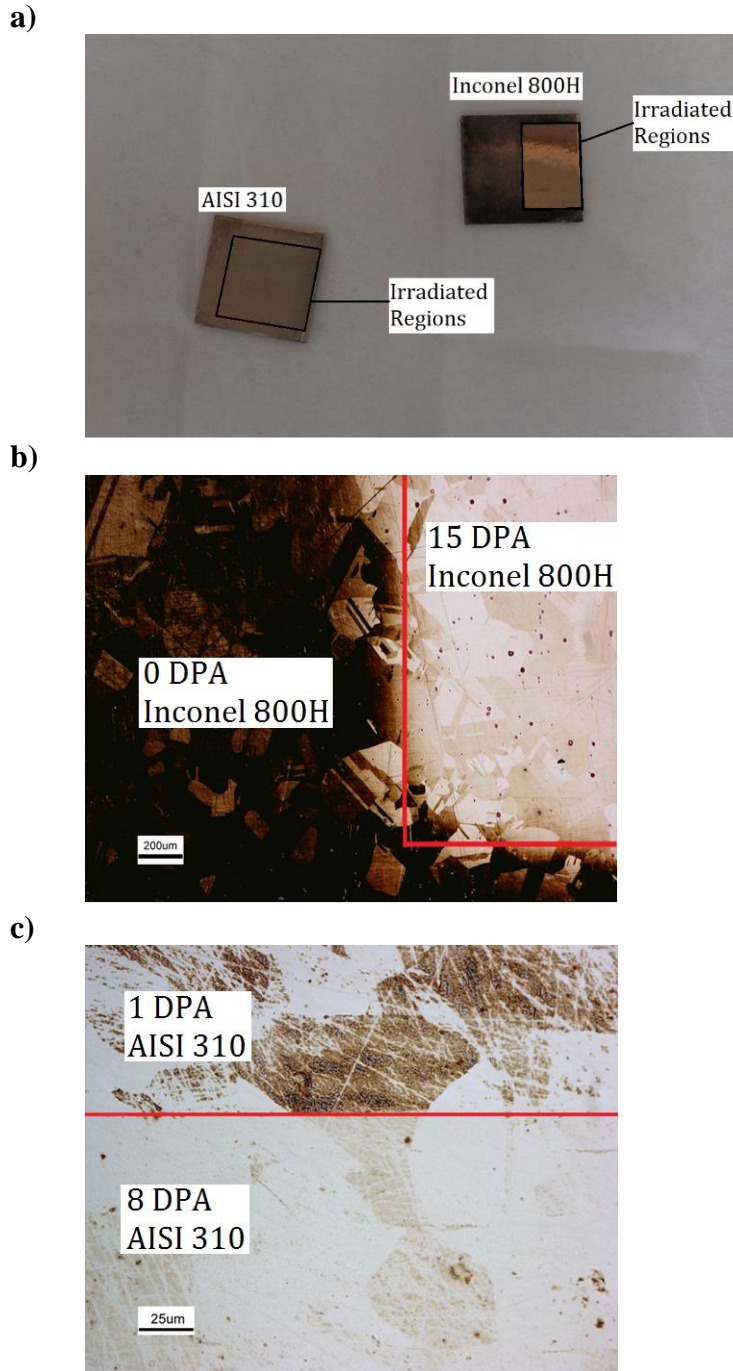


**Figure 4.7 Ion irradiated test samples exposed to 400° C for 1000 minutes. a) Optical low magnification images of AISI 310 (left) and Inconel 800H (right) b) High magnification, optical image of Inconel 800H sample c) High magnification, optical image of AISI 310 sample. These images show clearly that the extent of oxidation is reduced in regions exposed to high levels of ion irradiation.**

A realistic hypothesis<sup>3</sup> for the observation of thinner oxide formation in the ion-irradiated regions of the samples, is that the ion-induced crystal defects facilitate the diffusion of Cr to the free surface during high temperature exposure and this promotes a continuous chromium oxide layer passive layer to be maintained. This suggests alloys with a higher concentration of Cr will diffuse more Cr to the passivation layer, and thus suffer less surface oxidation. This logic is supported by the level of discolouration of AISI 310 (25% Cr) with respect to that of Inconel 800H (21% Cr) (Figure 4.7a). Further analyses of the chemical composition of the discoloured regions of the annealed ion-irradiated samples would be required to confirm this hypothesis.

Figure 4.8 shows typical hardness versus thermal recovery time data, at temperatures from 400 to 600° C, for our ion irradiated samples. These samples typically display an initial softening followed by a gradual hardening occurs with increased time at elevated temperature and the rate of increase is temperature dependent. This trend can be explained in terms of the simultaneous operation of two mechanisms: i) thermal recovery of irradiation-induced hardening and ii) increased hardening due to time-dependent growth of surface oxide. Based upon this hypothesis the events resulting in the hardness – time profiles displayed in Fig. 4.8 can be described as follows:

- 1) Before heating: The samples have increased hardness, relative to their non-irradiated counterpart, due to ion irradiation hardening and, to a small extent, residual work-hardening resulting from small amounts of surface polishing during the preparation stage.
- 2) After about 1 minute heating the samples have become much softer due to thermal recovery of much of the irradiation/polishing induced crystal damage. This suggests that much of the crystal damage is highly mobile and thus quickly recovered at elevated temperature.

---

<sup>3</sup> This hypothesis was suggested to us by Prof. J. Kish of McMaster University (April 2014).

3) After heating for longer duration samples begin to harden and display a visible surface oxide layer. The rate of hardening increases with increased heating temperature and with decreased Cr content in the test material (i.e. the Inconel 800H samples hardened more rapidly than the AISI 310 samples).

Our indentation data display the effect of these concurrent softening/hardening mechanisms. We are primarily interested in understanding the softening mechanism which occurs in the early stages of the thermal recovery process. In Chapter 5, we will develop a model to describe the thermal softening mechanism by analysing only the data from the early stages of the thermal recovery tests.

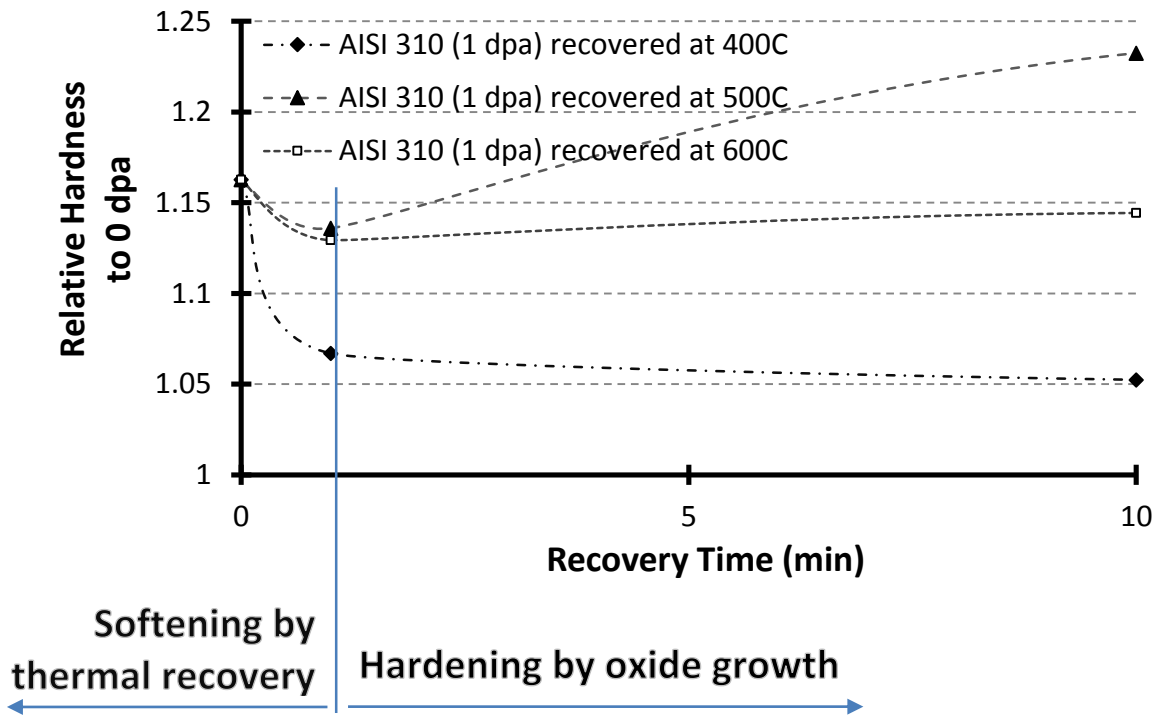


**Figure 4.8: Relative hardness for 1 dpa irradiated AISI 310 during 10 minutes of recovery. This shows softening occurred for the first minute from 400° to 600° C. After 1 minute, the samples recovering at 500° and 600° C harden. This phenomenon occurs for all irradiation levels, including non-irradiated samples, in both AISI 310 and Inconel 800H most strongly at 500° C. The 500° C was recovered with shorter purges, which correlates with the more intense hardening.**

# Chapter 5

## 5 Discussion

The data presented in Chapter 4 indicate clearly that the indentation hardness of the AISI 310 and the Inconel 800H alloys is dependent upon the parameters of indentation depth ( $h$ ), ion irradiation damage (dpa), annealing temperature ( $T$ ), and annealing time ( $t$ ). In this chapter we will assess the dependence upon each parameter separately. The end result of this analysis will be a series of equations that can be used to predict the hardness, and hence the yield stress ( $\sigma_{yield} \approx H/3$  [44]) of these alloys when they are subjected to in-core irradiation and temperature conditions envisioned for the Canadian Gen IV SCWR concept. A discussion of the limitations of our analysis will also be presented.

### 5.1 Effect of indentation depth on hardness

All the indentation hardness data from this study display clear indentation depth dependence (Figs. 4.1 - 4.6). What is presented here is an assessment of the indentation depth dependence of the hardness of the non-irradiated AISI 310 and Inconel 800H material. We limited our analysis to the non-irradiated material due to the highly depth dependent (Fig. 2.12) effect of ion irradiation on the local microstructure and thus the highly depth dependent hardness.

The effect indentation depth has on hardness is comparable to that of irradiation damage on these alloys. To segregate these effects would involve considerable uncertainty, which would mask the effect of both irradiation damage and the indentation depth dependence on hardness. Rather, we will examine the effect of ion irradiation and annealing on the hardness of these alloys at one indentation depth ( $h_p = 200\text{nm}$ ) in the subsequent Sections 5.2 and 5.3.

The indentation depth dependence of hardness of the non-irradiated AISI 310 and Inconel 800H material will be assessed by applying the model proposed by Nix and Gao [48] and

described in Section 2.4.3. The crux of the theory is the indentation hardness  $H$  should be linearly related to  $\sqrt{1/h_p}$  according to

$$\frac{H}{H_o} = \sqrt{1 + \frac{h^*}{h_p}} \quad 5.1$$

where  $H_o$  is the indentation hardness in the limit of infinite indentation depth and is therefore an intrinsic property of the indented material [48]. The characteristic length  $h^*$  is a property of the indenter shape and the indented material. Here we will analyse our data to determine first if they display a  $H-h_p$  dependence that is predicted by Equation 5.1 and, if so, how the parameters,  $H_o$  and  $h^*$ , differ between the AISI 310 and the Inconel 800H alloys and how they compare to published values for other alloys

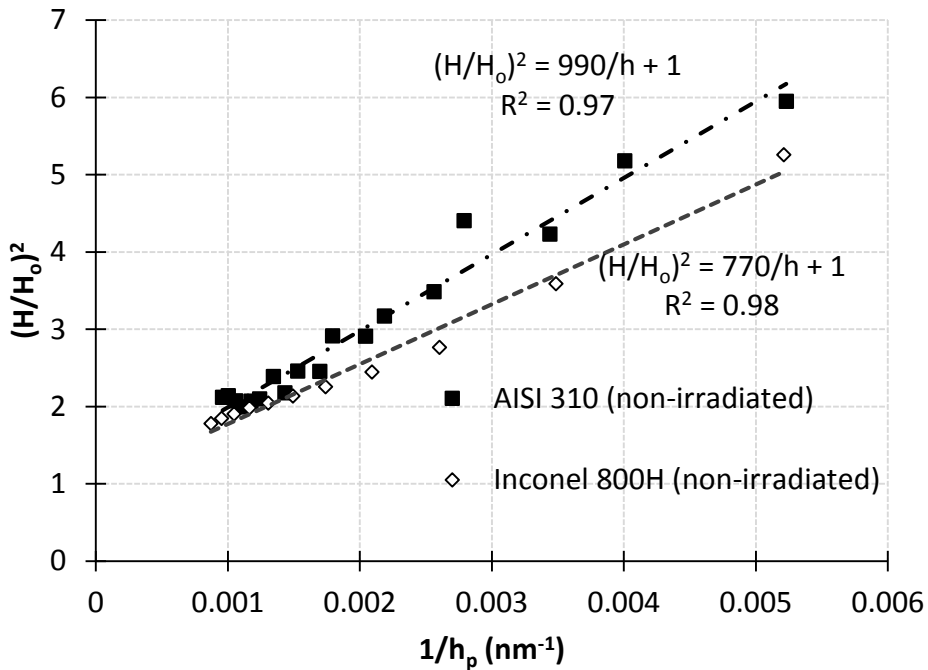


**Figure 5.1** Depth-hardness data from non-irradiated test samples plotted as  $\left(\frac{H}{H_o}\right)^2$  over  $\frac{1}{h_p}$  to examine the indentation depth dependence of hardness on the test materials.



**Table 5.1: Bulk hardness and characteristic length for various materials, including this experiments test materials, AISI 310 and Inconel 800H [48, 53, 54]**

Material	$H_o$ (GPa)	$h^*$ ( $\mu\text{m}$ )	Reference
(110) single crystal Ag	0.361	0.432	55
(100) single crystal Ag	0.34	0.757	55
(111) single crystal Cu (annealed)	0.581	1.60	48
Polycrystalline Cu (cold worked)	0.834	0.464	48
AISI 310	$1.7 \pm 0.3$	$1.0 \pm 0.3$	
Inconel 800H	$1.5 \pm 0.3$	$0.8 \pm 0.5$	
Deposited Ni film	n/a	2.451	56

This shows that the sample follow the trends predicted in the literature and have reasonable values compared to other published values for other metals.

## 5.2 Effect of ion irradiation on hardness

SRIM simulations indicate that the 8.0 MeV  $\text{Fe}^{4+}$  ions used in this study will penetrate, and create irradiation damage in, the sample to a depth of approximately  $2.0 \mu\text{m}$  (Figure 2.12, Section 2.2.2). We are therefore particularly interested in the hardness measured from indentation depths which have a plastic deformation zone extending no more than approximately  $2.0 \mu\text{m}$  from the surface of the sample (Figure 5.1).

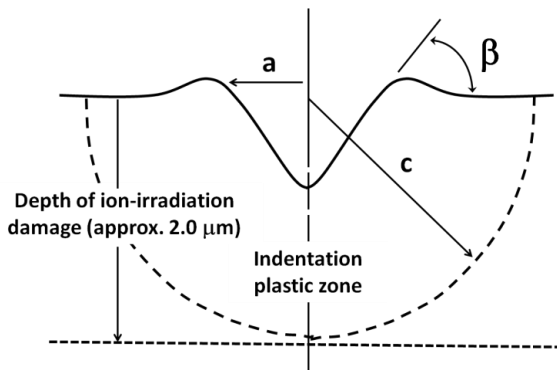


**Figure 5.2 Schematic illustration of a hemispherical plastic deformation zone, of radius  $c$ , around an indentation of width  $a$ .**

Applying the analysis put forth in Section 2.4.2, in which Equation 2.17, which is

$$c = \frac{h}{\tan(\beta)} \left[ \frac{E_R \tan \alpha}{6\sigma_y(1-\nu)} + \frac{2}{3} \left( \frac{1-2\nu}{1-\nu} \right) \right]^{1/3} \quad 5.2$$

using the values  $\beta = 20^\circ$ ,  $\nu = 0.36$ ,  $E_R = 184$  GPa, and  $\sigma_{y \text{ irradiated}} \cong 1.33$  GPa, we find that the radius  $c$  of the plastic zone is approximately 1.15, 2.31, and 4.61  $\mu\text{m}$  for indentation depths  $h$  of 100, 200, and 400 nm respectively. This suggested the relationship,  $c = 11.5h$ , which is close to  $c = 12h$ , which was calculated using elastic-plastic finite element analyses for pyramidal indentations of the same geometry as that used in this study [44 - 46].

Since the simulated depth of the ion-irradiation hardening in our study is about 2  $\mu\text{m}$  (Figure 2.12, Section 2.2.2), we will assess the effect of ion-irradiation on the hardness by considering the hardness data from indentation depths of 200 nm.

The average non-irradiated indentation hardness, at 200 nm depth, was 3.9 +/- 1.8 GPa and 6.8 +/- 1.7 GPa for the AISI 310 and the Inconel 800H alloys respectively. The scatter in the data indicates the effect of grain-to-grain variability and surface roughness of the test materials. Figure 5.3 shows the change in hardness ( $\Delta H$ ), at  $h = 200$  nm, versus the extent of ion irradiation damage (dpa). The parameter  $\Delta H$  is calculated as the increase in the average hardness relative to the average hardness of non-irradiated samples.

$$\Delta H_{h=200nm} = \frac{\bar{H}_{\text{irrad.}} - \bar{H}_{\text{nonirrad.}}}{\bar{H}_{\text{nonirrad.}}} \quad 5.3$$

For both alloys tested the indentation hardness at  $h_p = 200$  nm increases with irradiation very similarly to the irradiation of AISI 316LN by Fe ions as shown in Figure 5.3.

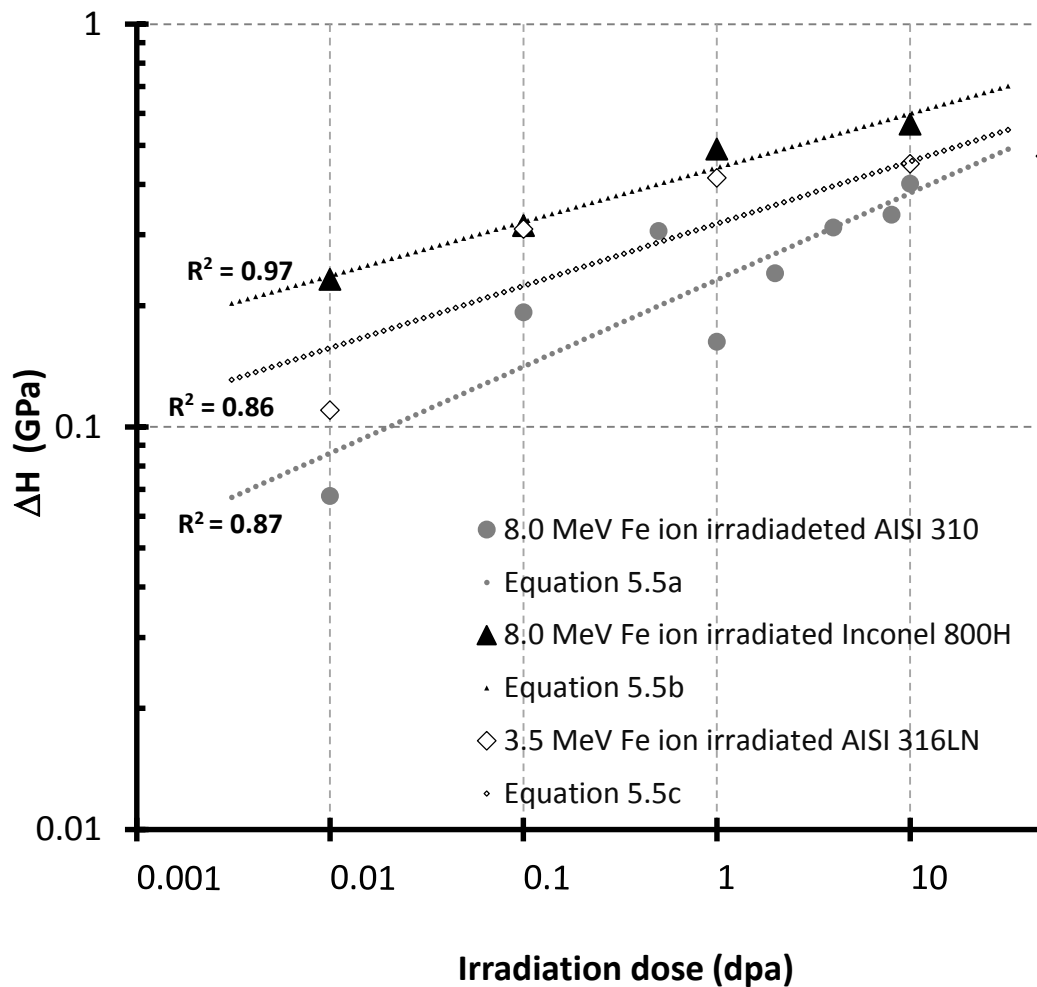


**Figure 5.3 Change in indentation hardness ( $\Delta H$ ) at 200 nm indentation depth, versus irradiation dose (displacements per atom or dpa) for the AISI 310 and Inconel 800H samples of this study. Data from Fe ion irradiated AISI 316LN reported by *Hunn et al.* [9] are also included in this plot. Trend lines for Equations 5.5a - 5.5c have been plotted alongside the data.**

The  $\text{Fe}^{4+}$  irradiation induces crystal defects, such as point defects and small dislocation loops, which are similar to the defects created by plastic deformation (i.e. cold working). The increase in hardness,  $\Delta H$ , resulting from a measure of cold work,  $CW$ , is often expressed by an equation of the form

$$\Delta H = a \times CW^b \quad 5.4$$

where  $a$  and  $b$  are experimentally derived coefficients. By taking the appropriate data and finding an equivalent curve of best fit for irradiation hardening, we can model  $\Delta H$  for AISI 310 and Inconel 800 as Equations 5.5a and 5.5b respectively. In these equations,  $\phi$  is the fluence in units of dpa and  $H_A$  is the annealed hardness.

$$\Delta H_{\phi, \text{ AISI 310}} = 0.27H_A\phi^{0.16} \quad (R^2 = 0.87) \quad 5.5a$$

$$\Delta H_{\phi, \text{ Inc 800H}} = 0.44H_A\phi^{0.12} \quad (R^2 = 0.97) \quad 5.5b$$

These two hardening trends fit the experimental data closely. They also show that typically Inconel 800H irradiation hardens much faster than AISI 310.

A similar analysis performed on the 150 nm indentation depth data provided by *Hunn et al.* on AISI 316LN (Figure 5.3) found the data could be modelled reasonably to

$$\Delta H_{\phi, \text{ AISI 316LN}} = 0.32H_A\phi^{0.13} \quad (R^2 = 0.86) \quad 5.5c$$

which closely resembles the coefficient and exponential values in Equations 5.5a and 5.5b (Table 2) [9].

**Table 5.2: Comparison of coefficient and exponential values to describe irradiation hardening of AISI 310 and Inconel 800H against the findings of *Hunn et al.* for AISI 316LN in the form of Equation 5.3. See Equations 5.5a - 5.5c. [9]**

Material	Coefficient value (a)	Exponential value (b)
AISI 310	0.26	0.16
Inconel 800H	0.44	0.12
AISI 316LN	0.32	0.13

The form of Equations 5.5a and 5.5b indicate that the rate of irradiation hardening ( $d\Delta H/d\phi$ ) continuously decreases with increasing irradiation damage ( $\phi$ ). This is intuitively reasonable, since ion-atom interactions create relatively simple and highly mobile crystal defects (such as vacancies, interstitials and small dislocation loops) whose high rate of recombination results in a balance being established between the rates of defect creation and annihilation at the higher levels of irradiation damage.

### 5.3 Thermal recovery

In the previous section we saw that the irradiation hardening followed a power-law dependence upon irradiation damage ( $\phi$ ), which varied for the different alloys studied. Large values of  $\phi$  reduced the rate of hardening to approximately zero. It was proposed that this indicated a steady-state condition where the rate of increase in irradiation damage equalled the rate of recovery of damage due to simple thermally activated mechanisms; such as vacancy-interstitial recombination.

In this section we study the kinetics of the thermally-activated recovery of the  $\text{Fe}^{4+}$  ion irradiation induced hardening. This study was done by measuring the indentation hardness of AISI 310 and Inconel 800H samples, at a depth of  $h_p = 200$  nm, for various levels of  $\text{Fe}^{4+}$  irradiation exposure (Table 3.2), after heating to temperatures of  $400^\circ$ ,  $500^\circ$ , and  $600^\circ$  C for various lengths of time. When choosing the lengths of time to be analysed we considered only data in the period where the indentation hardness was decreasing. Thus, we did not include data which displayed hardening resulting from the formation of surface oxide layers (see Section 4.3). Figure 5.4 shows the relative hardness,  $\hat{H}$ , given as

$$\hat{H} = H_{\text{irrad.}}/H_{\text{non-irrad.}} \quad 5.6$$

versus time throughout thermal recovery at  $400^\circ$  C.

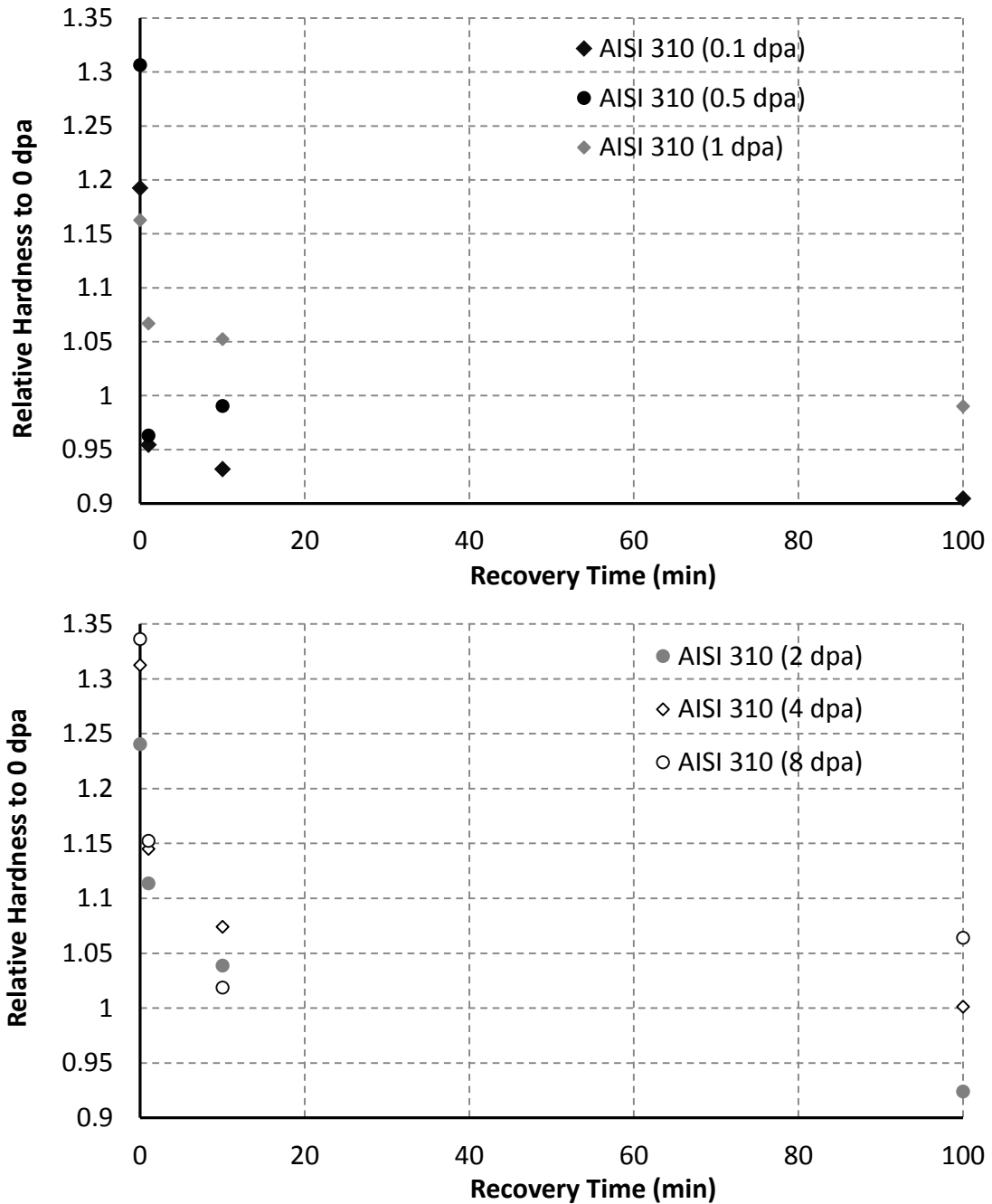


**Figure 5.4** Relative hardness for AISI 310 during recovery at 400° C. The plot show consistent softening towards the average non-irradiated, polished hardness. In the case of the 0.1 dpa hardness averaging below 1, this can be attributed to the removal of most of the irradiation hardening damage as well as the cold work from polishing which is present in all unrecovered hardness values.

### 5.3.1 Calculation of critical recovery time, $t_c$

Figure 5.4 indicated that the relative hardness displays an exponential dependence upon annealing time. Curves of the form

$$\hat{H}(t) = 1 + Ae^{nt} \quad 5.7$$

were fit to the data to find values of the parameters of  $A$  and  $n$  of each dpa level of ion irradiation for each sample (Table 5.3). The fitting was performed with a recursive algorithm searching for the two optimal parameters for each set of data to maximize the coefficient of determination ( $R^2$ ).

Some of these data found hardening occurred (italicized values of  $A$  and  $n$  in Table 5.3) instead of thermal recovery, which is evidence of surface oxidation occurring on the samples, as described in Section 4.3. This data has been excluded from use in further analysis to avoid underestimating thermal recovery by masking its effects with the hardening effect of surface oxidation. The lowest value for  $n$  is indicative of the instance with the least hardening from surface oxidation, and will thus be used to further mitigate the hardening effect of surface oxidation. These equations for  $\hat{H}(t)$  were then used to find the times required for near complete recovery of the irradiation damage,  $t_c$ . In other words, when  $t = t_c$ ,  $\hat{H}(t) \leq 1.01$ .

Table 5.3 lists the calculated values of  $A$  and  $n$  parameters of Equation 5.7 for AISI 310 and Inconel 800H samples irradiated to various dpa levels and annealed at the various temperatures. Note: italicized parameters indicate a hardening from thermal exposure. These values indicate high surface oxidation of the sample as described in Section 4.3. Bold parameters represent tests where surface oxidation was minimal. Bold data are used to predict the rate of thermal recovery of irradiation hardening.

Material	Temperature (° C)	Dose (dpa)	$A$	$n$ (min <sup>-1</sup> )
AISI 310	400	0.1	<b>0.37</b>	<b>-0.01</b>
AISI 310	400	0.5	<b>0.53</b>	<b>-0.07</b>
AISI 310	400	1	<i>0.46</i>	<i>0.00</i>
AISI 310	400	2	<b>0.52</b>	<b>-0.01</b>
AISI 310	400	4	<b>0.58</b>	<b>-0.01</b>
AISI 310	400	8	<i>0.58</i>	<i>0.00</i>
AISI 310	500	0.01	<i>0.44</i>	<i>0.15</i>
AISI 310	500	0.1	<b>0.58</b>	<b>-0.25</b>
AISI 310	500	1	<b>0.54</b>	<b>-0.07</b>
AISI 310	500	10	<b>0.85</b>	<b>-0.56</b>
AISI 310	600	0.01	<i>0.41</i>	<i>0.02</i>
AISI 310	600	0.1	<b>0.58</b>	<b>-0.34</b>
AISI 310	600	1	<b>0.54</b>	<b>-0.09</b>
AISI 310	600	10	<b>0.85</b>	<b>-0.35</b>
Inconel 800H	400	15	<b>0.42</b>	<b>-0.15</b>
Inconel 800H	500	0.01	<b>0.34</b>	<b>-2.03</b>
Inconel 800H	500	0.1	<b>0.43</b>	<b>-0.62</b>
Inconel 800H	500	1	<b>0.65</b>	<b>-0.69</b>
Inconel 800H	500	10	<b>0.70</b>	<b>-0.51</b>
Inconel 800H	600	0.01	<i>0.40</i>	<i>0.07</i>
Inconel 800H	600	0.1	<i>0.43</i>	<i>0.07</i>
Inconel 800H	600	1	<i>0.62</i>	<i>0.00</i>
Inconel 800H	600	10	<b>0.70</b>	<b>-0.13</b>

Excluding instances of hardening to find a mean value for  $A$  and  $n$ , we find the curves for each metal are,

$$\hat{H}_{AISI\ 310}(t) \cong 1 + 0.59e^{-0.14t} \quad 5.8a$$

$$\hat{H}_{Inc\ 800H}(t) \cong 1 + 0.54e^{-0.59t} \quad 5.8b$$



where time,  $t$ , is in units of minutes for AISI 310 and Inconel 800H respectively. By realising that the  $A$  parameter is the change in relative hardness, we can better describe these curves both as a function of irradiation damage (measured in dpa) as well as time.

Combining Equations 5.8a or 5.8b with Equations 5.5a - 5.6, we find

$$\hat{H}_{AISI\ 310}(t) = 1 + 0.26\phi^{0.16}e^{-0.14t} \quad 5.9a$$

$$\hat{H}_{Inc\ 800H}(t) = 1 + 0.44\phi^{0.12}e^{-0.59t} \quad 5.9b$$

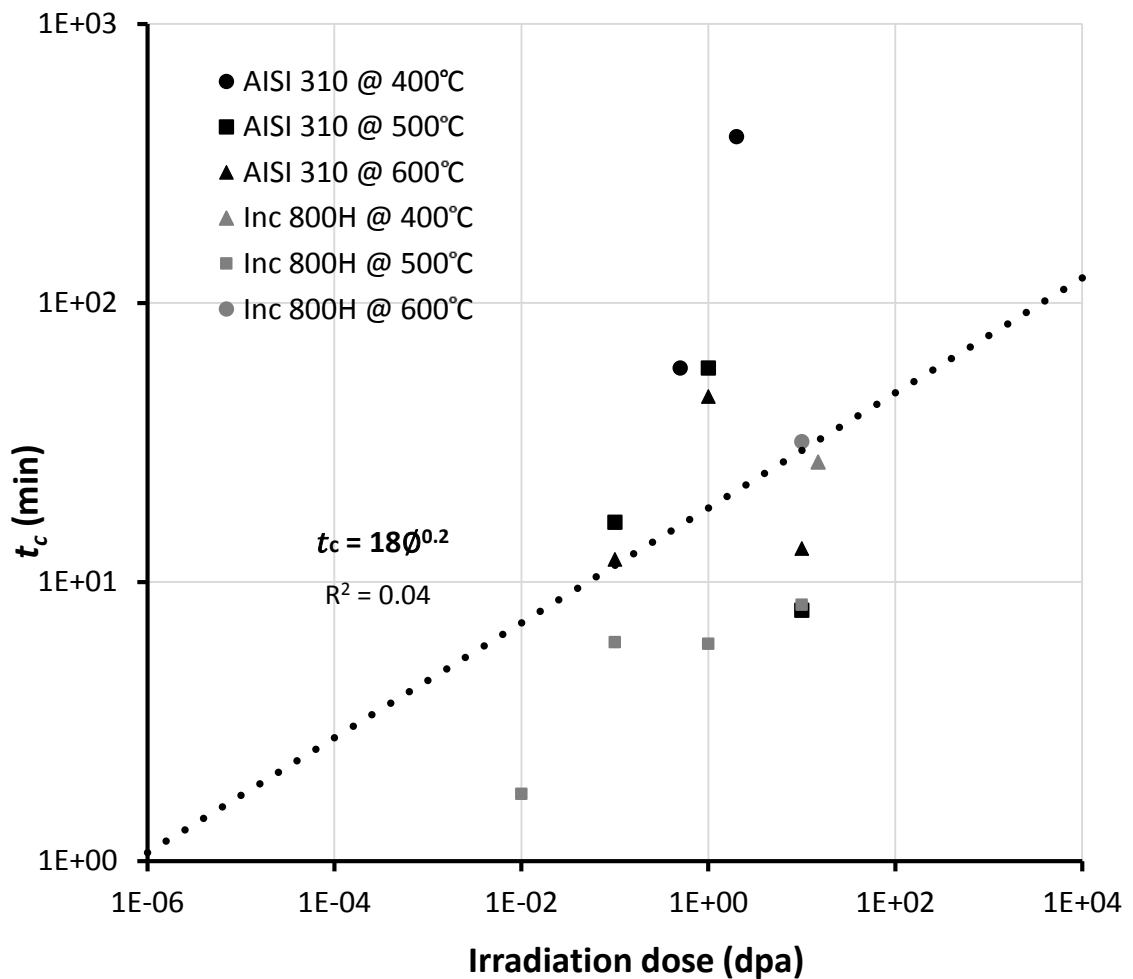


**Figure 5.5  $t_c$  versus irradiation dose (dpa) for AISI 310 and Inconel 800H during recovery, under the premise that  $t_c$  occurs when 99% of irradiation hardening has dissipated.**

Figure 5.5 depicts  $t_c$  as a function of irradiation dose through a log-log plot for both AISI 310 and Inconel 800H. Linear regression analysis of the data suggest the following functional relationship between  $t_c$  (minutes) and irradiation damage,  $\phi$ , (dpa):

$$t_c = 18\phi^{0.2} \quad 5.10$$

The data suggest that the rate of thermal recovery of ion-induced crystallographic damage is faster for Inconel 800H compared to AISI 310.

Included in Figure 5.6 are data from hardness tests performed on the AISI 310 alloy at 500° C. These data lie on the same trend as the 400° C data indicating that the rate of irradiation damage recovery is not significantly greater, within the precision limits of our measurement techniques, at 500° C or 600° C than at 400° C.

### 5.3.2 Model of the thermal recovery process

An alternate approach to characterizing the time-dependent recovery of ion irradiation damage in these alloys can be made by recognizing that the damage is primarily in the form of highly mobile point defects and small dislocation loops as described in Section 2.3 and [17]. We can express the rate at which hardness decreases over time as the product of the characteristic atomic jump frequency,  $\nu$  (given by Equation 2.9), and the recoverable hardness of a pre-irradiated material, which is the difference between the instantaneous hardness,  $H(t, T)$ , and the annealed the hardness of the material,  $H_A$ .

$$dH(t, T) = (H(t, T) - H_A)\nu dt \quad 5.11$$

where  $t$  is time and  $T$  is the absolute temperature. Integrating the change in hardness over time and applying the limit of  $t \rightarrow \infty$ , we find the that the integration constant will be  $H_A + \Delta H_\phi$ , as given by

$$H(t, T) = H_A + \Delta H_\phi - \int_0^t (H(t, T) - H_A)\nu dt \quad 5.12$$

By assuming temperature to be independent of time, Equation 5.12 can be simplified to

$$H(t, T) = H_A(1 + A + t\nu) - \nu \int_0^t H(t, T) dt \quad 5.13$$

Using Equations 5.6 - 5.7, we can integrate  $H(t, T) dt$  to find

$$H(t, T) = H_A \left( 1 + A - v \left( \frac{A}{n} e^{nt} - \frac{A}{n} \right) \right) \quad 5.14$$

where values for  $A$  and  $n$  are given in Table 5.3. By incorporating Equations 2.9 we have

$$H(t, T) = H_A \left( 1 + A - v_o e^{-\frac{q}{kT}} \left( \frac{A}{n} (e^{nt} - 1) \right) \right) \quad 5.15$$

We know  $A$ , which is  $\Delta H_\emptyset / H_A$ , is actually a function of irradiation dose,  $\emptyset$ , in dpa from Equations 5.5 – 5.7, and approximate values for  $n$  from the bold values in Table 5.3. These substitutions leave us with

$$H(t, T, \emptyset)_{AISI\ 310} = H_A \left( 1 + 0.26\emptyset^{0.16} + 1.8\emptyset^{0.16} v_o e^{-\frac{q}{kT}} (e^{-0.14t} - 1) \right) \quad 5.16a$$

$$H(t, T, \emptyset)_{Inc\ 800H} = H_A \left( 1 + 0.44\emptyset^{0.12} + 0.8\emptyset^{0.12} v_o e^{-\frac{q}{kT}} (e^{-0.59t} - 1) \right) \quad 5.16b$$

The Debye frequency,  $v_o$ , can be estimated for our Fe-Cr based alloys by using the speed of sound of stainless steel,  $v_s \cong 5800\ m/s$  [55] and the Debye model [56]

$$v_o = \left( \frac{3N}{4\pi V} \right)^{1/3} v_s \quad 5.17$$

where the atomic number density,  $\frac{N}{V}$ , is approximately  $8.5 \times 10^{28} \frac{atoms}{m^3}$ . This means for both alloys  $v_o \cong 9.5 \times 10^{14}\ min^{-1}$ .

Using the hardness data obtained from tests on the ion irradiated samples, the average activation energies,  $q$ , are  $2.3 \times 10^{-19}$  and  $3.7 \times 10^{-19} \frac{Joules}{atom}$  for the AISI 310 and Inconel 800H respectively. These values are very similar the  $q$  values given in literature for Ni – 20% Cr alloys of approximately  $4.7 \times 10^{-19} \frac{Joules}{atom}$  [57]. This leaves us with an equation describing hardness as a function of recovery time, recovery temperature, and irradiation dose for AISI 310 Inconel 800H.

$$H(t, T, \phi)_{AISI\ 310} = H_A \left( 1 + 0.26\phi^{0.16} + 1.8\phi^{0.16} e^{\frac{-16000}{T}} (e^{-0.14t} - 1) \times 10^{15} \right) \quad 5.18a$$

$$H(t, T, \phi)_{Inc\ 800H} = H_A \left( 1 + 0.44\phi^{0.12} + 7.1\phi^{0.12} e^{\frac{-19000}{T}} (e^{-0.59t} - 1) \times 10^{14} \right) \quad 5.18b$$

Physically, Equations 5.18a and 5.18b have 3 terms indicated by the terms within the outer brackets, all of which are functions of  $H_A$ . The first term simply expresses the annealed hardness of the test material. The second term represents the hardening that results from irradiation damage in the absence of thermal recovery. The sum of these two terms constitutes the hardness of the ion irradiated alloys before exposure to high temperature. The third term expresses the amount of hardness reduction resulting from exposure to an elevated temperature,  $T$ , for a time  $t$ . This third term approaches the second term in magnitude as  $t$  approaches infinity and indicates the case when all the irradiation hardening has been recovered.

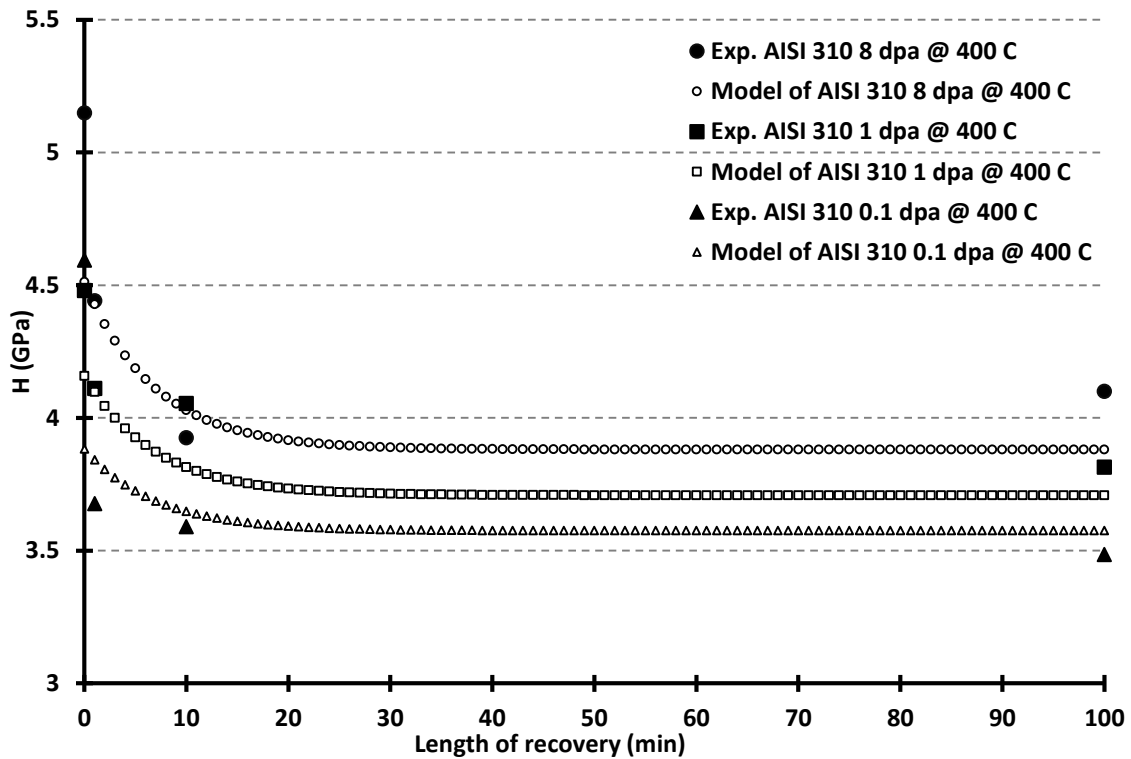


**Figure 5.6 A comparison of the experimental AISI 310 data and the model for AISI 310 (Equation 5.18a)**

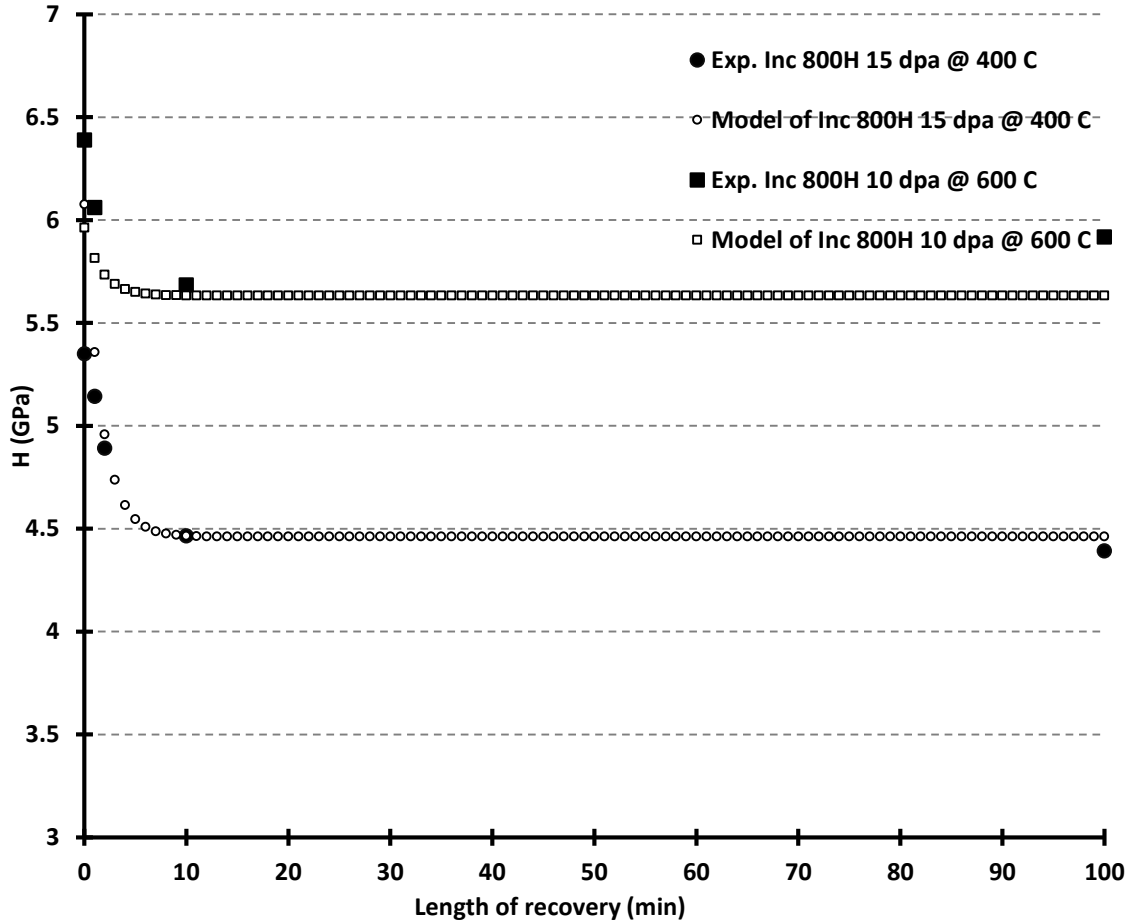


**Figure 5.7 A comparison of the experimental Inconel 800H data and the model for Inconel 800H (Equation 5.18b)**

Figures 5.6 and 5.7 show the experimental data for AISI 310 and Inconel 800H, respectively, in comparison to our models, Equations 18a and 18b. Figure 5.6 and 5.7 shows our models fit the data well. This shows our model accurately predicts the irradiation hardening and the thermal recovery of this hardening. This indicates that our methodology of irradiation followed by thermal recovery, as opposed to in-situ testing, was successful.

## 5.4 Testing issues and their effects

After exposure to elevated temperature the samples in this study typically displayed some amount of surface discolouration (See Section 4.3). The amount of discolouration increased with time and annealing temperature. The tendency to become discoloured was also material dependent with the Inconel 800H alloy becoming more quickly discoloured than the AISI 310 alloy. These observations are all consistent with the samples becoming oxidized during the annealing treatments. An interesting observation from this study was that the amount of discolouration (i.e. oxidation) was dramatically dependent upon the level of prior ion irradiation with less discolouration occurring on the highly ion-irradiated regions of the samples (Figure 4.7).

The presence of metal oxides on the heated samples affects the measured indentation hardness as shown by the italicized data in Table 5.3: When the oxide layer grows in thickness, at small indentation depth of 200 nm the measured hardness is increased. Figure 4.8 shows an initial softening followed by a hardening occurs in samples when they are thermally heated above 400° C for up to 100 minutes. This trend occurs in all irradiated samples heated over 400° C and in some cases the material is harder after heating.

The effect ion irradiation has on oxidation resistance can be explained by the hypothesis described in Section 4.3 and indicates that ion irradiation damage, like vacancies and interstitials, facilitates enhances Cr diffusion to occur to the surface of the sample resulting in enhanced surface passivation (Section 2.3).

## Chapter 6

### 6 Conclusions

The Canadian supercritical water fission reactor concept should increase the thermal efficiency of nuclear power generation to approximately 48% primarily by operating the reactor core at considerably elevated temperatures compare to existing reactors. Currently, the largest design constraint of this project is the lack of data on the strength of selected alloys in the presence of high temperature neutron irradiation. This thesis examines irradiation hardening and thermal recovery over the elevated temperature range from 400° C to 600° C of two candidate alloys, AISI 310 and Inconel 800H, for the Canadian SCWR concept.

Samples of both alloys were mechanically ground and polished, then irradiated using 8.0 MeV Fe<sup>4+</sup> ions to simulate neutron irradiation. Samples were then heated at temperatures ranging from 400° to 600° C to measure the rate of thermal recovery of their indentation hardness.

These test results have shown that ion irradiation damage does create significant amounts of crystallographic damage, resulting in an increased hardness, in both tested alloys. Most of this damage is very mobile, in the form of point defects and small dislocation loops. The mobile nature of the irradiation damage makes nearly complete thermal recovery possible within 100 minutes at 400° C.

Equations were developed to describe the hardness of both alloys: i) immediately after irradiation of dose  $\emptyset$ , (Equations 5.5a, 5.5b) ii) after  $t$  minutes at temperature  $T$ , (Equations 5.18a, 5.18b) and iii) the critical time  $t_c$  for complete recovery (Equation 5.10). The models for hardness immediately after irradiation of dose  $\emptyset$  fit the data well for both alloys, and more so are very similar to data from other reported tests (Figure 5.3). The models predicting hardness after irradiated samples are exposed to high temperatures also fits the data very well. This validates our hypothesised testing technique. The equation for critical time fit the experimental data to within an order of magnitude, finding doses as high as 10 dpa could be recovered typically within an hour.

Our findings suggest that in the case of high-temperature in-core applications, typical of those being proposed for fuel cladding and pressure tube liners in Canada's Gen-IV SCWR concept, both AISI 310 and Inconel 800H alloys will undergo at least 20% increase in hardness as a result of low levels of neutron irradiation damage typical of what could be expected within one year in core<sup>4</sup>. This hardness increase will however be negated by very rapid concurrent thermal recovery. Our data suggest that the recovery rate is sufficiently rapid that no noteworthy net irradiation hardening will occur in the Gen. IV SCWR fuel channel components.

Another important other factor that will affect the actual rate of irradiation hardening and thermal recovery in these alloys is the rate of hardening resulting from accumulated hydrogen and helium transmutation products. Our study did not address this issue.

Our study also revealed that tests conducted at 500° and 600° C formed surface oxides. This suggests that future test should be performed in furnace conditions with lower oxygen content; perhaps the use of a vacuum furnace or using a reducing gas, such as Ar-2.5%H, in lieu of the inert gas, Ar, which was used in this study. The tests showed some work hardening was present in the polished sample surfaces, suggesting future tests should employ electrochemical polishing techniques or in-vacuum annealing prior to implantation within the ion-implantation chamber.

---

<sup>4</sup> Fuel channel components typically experience about 1 dpa of irradiation damage per year of reactor operation [26].



## Works Cited

- [1] World Nuclear Association, "Nuclear Power Reactors," November 2013. [Online]. Available: <http://www.world-nuclear.org/info/nuclear-fuel-cycle/power-reactors/nuclear-power-reactors/>. [Accessed 12 June 2014].
- [2] M. Finkenrath, "[http://www.iea.org/publications/freepublications/publication/costperf\\_ccs\\_powergen-1.pdf](http://www.iea.org/publications/freepublications/publication/costperf_ccs_powergen-1.pdf)," International Energy Association, 2011. [Online]. Available: [http://www.iea.org/publications/freepublications/publication/costperf\\_ccs\\_powergen-1.pdf](http://www.iea.org/publications/freepublications/publication/costperf_ccs_powergen-1.pdf). [Accessed 12 June 2014].
- [3] M. Yetisir, M. Gaudet and D. Rhodes, "Development and Intergration of Canadian SCWR Concept with Counter-Flow Fuel Assembly," in *6th International Symposium on Supercritical Water-Cooled Reactors*, Shenzhen, 2013.
- [4] The International Association for the Properties of Water and Steam, "Guideline on the Use of Fundamental Physical Constants," International Association for the Properties of Water and Steam, Gaithersburg, 2001.
- [5] R. B. Duffey and L. K. H. Leung, "Advanced Cycle Efficiency: Generating 40% More Power from the Nuclear Fuel," in *Proceeding World Energy Congress (WEC)*, Montreal, 2010.
- [6] S. B. Krivit, T. B. Kingery and J. H. Lehr, *Nuclear Energy Encyclopedia: Science, Technology, and Applications*, Hoboken: John Wiley & Sons, Inc., 2011.
- [7] P. Kritzer, "Corrosion in high-temperature and supercritical water and aqueous solutions: a review," *The Journal of Supercritical Fluids*, vol. 29, no. 1-2, pp. 1-29, 2004.
- [8] Aquitaine Electronique et Informatique, *Java-based Nuclear Information Software 4.0 (software)*, OECD and NEA, 2013.

- [9] J. D. Hunn, E. H. Lee, T. S. Byun and L. K. Mansur, "Helium and Hydrogen Induced Hardening in 316LN Stainless Steel," *Journal of Nuclear Materials*, vol. 282, pp. 131-136, 2000.
- [10] M. Griffiths, "The Effect of Irradiation on Ni-Containing Components IN CANDU Reactor Cores: A Review," *AECL Nuclear Review*, vol. 2, no. 1, pp. 1-16, 2013.
- [11] Rolled Alloys Canada, "800H/AT," Rolled Alloys Canada, 2015. [Online]. Available: <http://www.rolledalloys.ca/alloys/nickel-alloys/800h-at/en/>. [Accessed 4 March 2015].
- [12] Rolled Alloys Canada, "310," Rolled Alloys Canada, 2015. [Online]. Available: <http://www.rolledalloys.ca/alloys/stainless-steels/310/en/>. [Accessed 4 March 2015].
- [13] L. E. Steele and J. R. Hawthorne, "Neutron Embrittlement of Reactor Pressure Vessel Steels," MIT Technology Press, Cambridge, 1963.
- [14] G. R. Odette and G. E. Lucas, "Irradiation Embrittlement of Reactor Pressure Vessel Steels: Mechanisms, Models, and Data Correlations," *ASTM STP 909*, pp. 206-241, 1986.
- [15] F. A. Garner, "In Phase Stability During Irradiation," in *Proceedings of the Symposium of the AIME*, Pittsburgh, 1980.
- [16] A. D. Marwick, R. C. Piller and M. E. Horton, in *Proc. Conf. on Dimensional Stability and Mechanical Behaviour of Irradiated Metals and Alloys*, London, 1984.
- [17] Y. Idrees, *Microstructural Evolution in Zr and Zr Alloy Excel under Ion Irradiation*, Kingston: McGill-Queen's University Press, 2013.

- [18] E. P. Wigner, "Theoretical Physics in the Metallurgical Laboratory of Chicago," *Journal of Applied Physics*, vol. 17, no. 11, pp. 857-863, 1946.
- [19] M. T. Robinson, "Basic physics of radiation damage production," *Journal of Nuclear Materials*, vol. 216, pp. 1-28, 1994.
- [20] E. M. Grieveson, D. E. J. Armstrong, S. Xu and S. G. Roberts, "Compression of self-ion implanted iron micropillars," *Journal of Nuclear Materials*, vol. 430, no. 1-3, pp. 119-124, 2012.
- [21] C. Heintze, C. Recknagel, F. Bergner, M. Hernández-Mayoral and A. Kolitsch, "Ion-irradiation-induced Damage of Steels Characterized by Means of Nanoindentation," *Nuclear Instruments and Methods in Physics Research Section B: Beam Interactions with Materials and Atoms*, vol. 267, no. 8-9, pp. 1505-1508, 2009.
- [22] D. E. J. Armstrong, A. J. Wilkinson and S. G. Roberts, "Mechanical properties of ion-implanted tungsten-5 wt% tantalum," *Physica Scripta*, vol. 2011, no. T145, p. 014076, 2011.
- [23] D. E. J. Armstrong, X. Yi, E. A. Marquis and S. G. Roberts, "Hardening of self ion implanted tungsten and tungsten 5-wt% rhenium," *Journal of Nuclear Materials*, vol. 432, pp. 428-436, 2013.
- [24] F. M. Halliday, D. E. J. Armstrong, J. D. Murphy and S. G. Roberts, "Nanoindentation and Micromechanical Testing of Iron-Chromium Alloys Implanted with Iron Ions," *Advanced Materials Research*, vol. 59, pp. 304-307, 2008.

- [25] C. Heintze, F. Bergner and M. Hernández-Mayoral, "Ion-irradiation-induced damage in Fe-Cr alloys characterized by nanoindentation," *Journal of Nuclear Materials*, vol. 417, no. 1, pp. 980-983, 2011.
- [26] B. Bose, Assessment of the Kinetics of Local Plastic Deformation of Zr-2.5%Nb CANDU Pressure Tube Material, London: The Althouse Press, 2012.
- [27] M. Nastasi, J. Mayer and J. Hirvonen, Ion-Solid Interactions: Fundamentals and Applications, Cambridge: Cambridge University Press, 1996.
- [28] P. Hosemann, C. Vieh, R. R. Greco, S. Kabra, J. A. Valdez, M. J. Cappiello and S. A. Maloy, "Nanoindentation on ion irradiated steels," *Journal of Nuclear Materials*, vol. 389, no. 2, pp. 239-247, 2009.
- [29] R. O. Oviasuyi, Investigation of the use of Micro-Mechanical Testing to Analyze the Mechanical Anisotropy of the Zr-2.5%Nb Pressure Tube Alloy, London: The Althouse Press, 2012.
- [30] J. F. Ziegler, M. D. Ziegler and J. P. Biersack, "SRIM - The stopping and range of ions in matter," *Nuclear Instruments and Methods in Physics Research Section B*, vol. 268, no. 11-12, pp. 1818-1823, 2010.
- [31] S. Fitzgerald, "Radiation damage I," 17 November 2013. [Online]. Available: [http://defects.materials.ox.ac.uk/uploads/files/Radiation\\_Damage\\_Lecture\\_1.pdf](http://defects.materials.ox.ac.uk/uploads/files/Radiation_Damage_Lecture_1.pdf). [Accessed 3 March 2015].
- [32] J. F. Shackelford, Introduction to Materials Science for Engineers (Third Edition), New York: Macmillan Publishing Company, 1992.
- [33] M. R. Gilbert, S. L. Dudarev, S. Zheng, L. W. Packer and J. C. Sublet, "Transmutation, gas production, and helium embrittlement in materials under neutron irradiation.," *Culhan Centre For Fusion Energy*, vol. 2, 2012.

- [34] L. Greenwood, "A new calculation of thermal neutron damage and helium production in nickel," *Journal of Nuclear Materials*, vol. 115, no. 2-3, pp. 137-142, 1983.
- [35] C. Dethloff, *Modeling of Helium Bubble Nucleation and Growth in Neutron Irradiated RAFM Steels*, KIT Scientific Publishing, 2012.
- [36] K. Ehrlich, "The development of structural materials for fusion reactors," *Philosophical Transactions A*, vol. 357, pp. 595-623, 1999.
- [37] M. Ashby, H. Shercliff and D. Cebon, *Materials: engineering, science, processing and design*, Oxford: Elsevier, 2007.
- [38] R. Balluffi, S. Allen and W. Carter, *Kinetics of Materials*, Hoboken: John Wiley & Sons Inc., 2005.
- [39] R. Abbaschian, L. Abbaschian and R. E. Reed-Hill, *Physical Metallurgy (Fourth Edition)*, Stamford: Cengage Learning, 2009.
- [40] A. C. Fischer-Cripps, "A review of analysis methods for sub-micron," *Vacuum*, vol. 58, pp. 569-585, 2000.
- [41] D. Tabor, "The Hardness of Metals," Oxford, OUP Oxford, 2000, p. 188.
- [42] A. C. Fischer-Cripps, *Nano-indentation*, New York: Springer Science & Business Media, 2004.
- [43] K. L. Johnson, "The Correlation of Indentation Experiments," *Journal of the Mechanics and Physics of Solids*, vol. 18, no. 2, pp. 115-126, 1970.
- [44] D. Tabor, *DEFORMATION OF METALS BY SPHERICAL INDENTERS*, Oxford: Clarendon Press, 1951.

- [45] Y. Murakami and M. Itokazu, "Elastic-plastic analysis of a triangular pyramidal indentation," *International journal of solids and structures*, vol. 34, pp. 4005-4018, 1997.
- [46] P. -L. Larsson, A. E. Giannakopoulos, E. Söderlund, D. J. Rowcliffe and R. Vestergaard, "Analysis of Berkovich indentation," *International Journal of Solids and Structures*, pp. 221-248, 1996.
- [47] N. A. Fleck, G. M. Muller, M. F. Ashby and J. W. Hutchinson, "Strain Gradient Plasticity: Theory and Experiment," *Acta Metallurgica et Materialia*, vol. 42, no. 2, pp. 475-487, 1994.
- [48] W. D. Nix and H. Gao, "Indentation size effects in crystalline materials: A law for strain gradient plasticity," *Journal of the Mechanics and Physics of Solids*, vol. 46, no. 3, pp. 411-425, 1998.
- [49] K. W. McElhane, J. J. Vlassak and W. D. Nix, "Determination of indenter tip geometry and indentation contact area of depth-sensing indentation experiments," *Journal of Materials Research*, vol. 13, no. 5, pp. 1300-1306, 1998.
- [50] N. A. Stelmashenko, M. G. Walls, L. M. Brown and Y. V. Milman, "Microindentations on W and Mo oriented single crystals: An STM study," *Acta Metallurgica et Materialia*, vol. 25, no. 4, pp. 2855-2865, 1993.
- [51] M. Haghshenas, *Micro-mechanical assembly of the local plastic strain invoked during a splined mandrel flow forming operation*, London: The Althouse Press, 2013.
- [52] J. Hendricks, Interviewee, *Research Technician*. [Interview]. 25 March 2015.
- [53] Q. Ma and D. R. Clarke, "Size dependent hardness in silver single crystals," *Journal of Materials Research*, vol. 10, pp. 853-863, 1995.

- [54] S. Graça, R. Colaço, P. A. Carvalho and R. Vilar, "Determination of dislocation density from hardness measurements in metals," *Materials Letters*, vol. 62, no. 23, pp. 3812-3814, 2008.
- [55] Class Instrumentation Ltd., "Class Instrumentation Ltd Ultrasonic Sound Velocity Table," Class Instrumentation Ltd., 2013. [Online]. Available: [http://www.classltd.com/sound\\_velocity\\_table.html](http://www.classltd.com/sound_velocity_table.html). [Accessed 16 July 2015].
- [56] T. L. Hill, *An Introduction to Statistical Thermodynamics*, New York: Dover Publications, 1987.
- [57] H. J. Frost and M. F. Ashby, *Deformation-Mechanism Maps: The Plasticity and Creep of Metals and Ceramics*, Oxford: Pergamon Press, 1982.

# HEYGAAN RAJAKUMAR

---

---

## ENGINEERING EXPERIENCE

---

M.E.Sc. CANDIDATE, UWO, London, ON May 2012 to September 2015

- Modelled irradiation hardening and thermal recovery of alloys for use in next generation fission reactor cores
- Performed metallurgical and mechanical testing
- Built and maintained lab equipment for safe use in experiments
- Supervised and trained multiple students in day-to-day tasks and safety procedures
- Scheduled project activities and milestones
- Worked with consultants, vendors, other departments, and other universities
- Created and presented seminars at conferences, meetings, and departmental seminars

TEACHING ASSISTANT, UWO, London, ON May 2012 to August 2014

- Instructed undergraduate students in coursework for Materials Science, Nuclear Engineering, and Mechatronics
- Supervised exams, tutorial sessions, laboratory experiments
- Assisted with laboratory set up

LOGISTICS ENGINEER, GDLS - Canada, London, ON August 2011 to April 2012

- Investigated maintenance and survivability of components and assemblies of light armored vehicles for the U.S. Army and the U.S. Marine Corps.
- Compiled information packages and wrote technical literature for field vehicle maintenance
- Sourced parts to be used for repair and replacement kits

JUNIOR DESIGNER, Diamond Aircraft, London, ON May 2008 to August 2009

- Assisted with the airframe ice protection systems and fuel system development for a jet aircraft
- Created 3D models, detailed drawings, technical layouts using CATIA V5
- Provided problem solving expertise to manufacturing team, operations and other departments
- Performed design calculations and trade-off studies



---

---

**EDUCATION**

---

MASTER OF ENGINEERING SCIENCE Graduating September 2015  
MECHANICAL ENGINEERING  
University of Western Ontario

BACHELOR OF ENGINEERING SCIENCE April 2011  
MECHANICAL ENGINEERING  
University of Western Ontario

**RELEVANT SKILLS**

---

Proficient with:

- MS Office (Word, PowerPoint, Excel)
- Visual Basic Script, MatLab, C++
- SolidWorks, CATIA, Unigraphics NX

**RELEVANT COURSEWORK/TRAINING**

---

NUCLEAR ENGINEERING

- Learned CANDU reactor operation and engineering
- Studied health physics and radiation protection
- Examined methods of controlling a nuclear fission reaction

TECHNICAL COMMUNICATIONS

- Developed professional presentation skills
- Learned technical report writing skills

PRODUCT DESIGN AND DEVELOPMENT

- Developed orientation to design for product safety, manufacturability, and assembly
- Practiced design simulations and analysis techniques

SCIENCE & TECHNOLOGY OF SUPERCRITICAL WATER REACTORS

- International Atomic Energy Association course taught at McMaster University (2012)
- Examined thermodynamics, neutronics, fluid mechanics and material science effects of conventional CANDU plants and the effects of supercritical water as a coolant

**AWARDS**

---

- Dean's Honor List April 2005

---

**TECHNICAL SEMINARS & PUBLICATIONS**

---

R. Klassen, H. Rajakumar, "*Combined effect of irradiation and temperature on the mechanical strength of Inconel 800H and AISI 310 alloys for in-core components of a GEN-IV SCWR*", accepted, available online at <http://nuclearengineering.asmedigitalcollection.asme.org/article.aspx?articleid=2396644>, (Paper NERS-15-1077), ASME, Journal of Nuclear Engineering and Radiation Science (2015).

R. Klassen, H. Rajakumar, "*Combined Effect of Irradiation and Temperature on the Mechanical Strength of Inconel 800H and AISI 310 alloys for in-core components of a Gen-IV SCWR*", the 7<sup>th</sup> International Symposium on Supercritical Water-Cooled Reactors (Helsinki, Finland 2015).

H. Rajakumar, "*Irradiation Damage and the Thermal Recovery of Alloys for Gen. IV SuperCritical Water Reactors*", Mechanical Engineering Graduate Seminar Series (London, 2014).

H. Rajakumar, R. Klassen, "*Effect of Temperature and Ion Irradiation on the Mechanical Properties of Materials for Gen. IV Supercritical Water Reactor*", Material Science & Technology Conference (Montreal, 2013).

H. Rajakumar, R. Klassen, "*Effect of Temperature and Ion Irradiation on the Mechanical Properties of Materials for Gen. IV Supercritical Water Reactor*", Canadian Material Science Conference (Montreal, 2013).

E. Savory, S. Gholamreza-Kashi, I. Naqavi, H. Rajakumar, R. Martinuzzi, "*Experimental and Numerical Modeling of Flow and Dispersion in a Horizontal, Non-Buoyant, Turbulent Surface Jet*", PHYSMOD 2009 (Sint-Genesius-Rode, 2009).